


Ferroically Ordered Magnetic Octupoles in d -Wave Altermagnets

Syantika Bhowal¹ and Nicola A. Spaldin¹

Materials Theory, ETH Zurich, Wolfgang-Pauli-Strasse 27, 8093 Zurich, Switzerland

 (Received 18 January 2023; revised 11 September 2023; accepted 22 December 2023; published 15 February 2024)

We show that time-reversal symmetry-broken, centrosymmetric antiferromagnets with nonrelativistic spin splitting of d -wave symmetry—the so-called d -wave *altermagnets*—are conveniently described in terms of the ferroic ordering of magnetic octupoles. The magnetic octupoles are the lowest-order ferroically ordered magnetic quantity in this case and so are the natural order parameter for the transition into the magnetically ordered state. They provide a unified description of the broken time-reversal symmetry and the nonrelativistic spin splitting, as well as a platform for manipulating the latter, and account for other phenomena, such as piezomagnetism, characteristic of this class of antiferromagnets. Unusually for antiferromagnets, we show that the magnetic octupoles cause a nonzero magnetic Compton scattering, providing a route for their direct experimental detection. We illustrate these concepts using density-functional and model calculations for the prototypical nonrelativistic spin-split antiferromagnet, rutile-structure manganese difluoride MnF_2 .

DOI: [10.1103/PhysRevX.14.011019](https://doi.org/10.1103/PhysRevX.14.011019)

Subject Areas: Condensed Matter Physics,
Magnetism, Spintronics

I. INTRODUCTION

The behavior that we now know as antiferromagnetism was first noticed around 100 years ago, when peaks in both specific heat and magnetic susceptibility were observed in materials such as MnO that have zero net magnetic moment [1,2]. Soon after, Néel proposed a model in which local magnetic dipole moments of equal magnitude on two sublattices order in an antiparallel fashion [3]. While the predictions of the Néel model were consistent with the observations [4], another ten years elapsed before neutron diffraction provided the first direct evidence of antiferromagnetic ordering of magnetic dipoles [5].

Usually, the order parameter \vec{L} of an antiferromagnet (AFM) is defined in terms of the difference between the local magnetic dipole moments \vec{M}_1 and \vec{M}_2 on the two sublattices: $\vec{L} = \vec{M}_1 - \vec{M}_2$. Such a definition is conceptually intuitive but lacks the convenience provided by ferroic order parameters such as the magnetization \vec{M} in ferromagnets or the electric polarization \vec{P} in ferroelectrics. For example, the Néel vector does not provide information about the conjugate field required to select for a particular antiferromagnetic domain and fails to distinguish between antiferromagnets that do or do not break time-reversal

symmetry. The magnetic dipoles, however, are just one of the terms in a multipole expansion of the energy of a general magnetization density in a magnetic field. They are generally the lowest-order local multipole on an atomic site, which makes them appealing for classifying magnetic order, but there is no fundamental reason why they should necessarily be the best choice. In particular, when the magnetic dipoles order antiferromagnetically, higher-order multipoles that order ferroically might be more suitable [6].

Indeed, such a higher-order-multipole description is now established in the case of AFMs that break both time-reversal (\mathcal{T}) and space-inversion (\mathcal{I}) symmetries and which are classified by the ferroic ordering of their local magnetoelectric multipoles [7–9]. The magnetoelectric multipoles make up the next-order term, beyond the magnetic dipoles, in the multipole expansion of the magnetic interaction energy [see Eq. (1)] and so depend linearly on both position r and magnetization density μ . Note that here (and throughout the manuscript) we refer to the *global* \mathcal{T} symmetry breaking, for which neither time reversal nor time reversal plus translation is a symmetry operation. All such \mathcal{T} - and \mathcal{I} -broken insulating AFMs with ferroically ordered magnetoelectric multipoles, therefore, exhibit a linear magnetoelectric response, in which an applied electric field induces a magnetization linear in the field strength and vice versa [10]. Their conjugate field is the product of electric and magnetic fields, which is exploited in so-called magnetoelectric annealing to select for a particular antiferromagnetic domain in magnetoelectric devices [11,12]. The ferroic ordering of magnetoelectric multipoles also plays a crucial role in antiferromagnetic

Published by the American Physical Society under the terms of the Creative Commons Attribution 4.0 International license. Further distribution of this work must maintain attribution to the author(s) and the published article's title, journal citation, and DOI.

spintronics [13–15] and skyrmionics [16,17] and can give rise to unconventional transport properties [18].

Recently, there has been renewed interest in a class of magnets with zero net magnetization that break time-reversal symmetry and exhibit a spin splitting of their energy bands that is not of relativistic origin (in conventional antiferromagnets, the bands are doubly spin degenerate). The nonrelativistic spin splitting (NRSS) is found to be substantial, in fact much larger than relativistic Rashba-like spin splitting [19–21], in some antiferromagnetic materials containing only light elements. An important recent development was the articulation of guiding principles for realizing such unconventional magnetism in materials [22–30], in particular, the use of spin-group theory to classify the pattern of the spin splitting as *d*-, *g*-, or *i*-wave [28], so that associated unconventional properties of both fundamental and technological importance [28,31], including efficient spin-current generation [32–34], spin-splitting torque [35,36], giant magnetoresistance [37], spontaneous Hall effect [22,38–41], superconductivity [42], and chiral magnons [43], could now be within reach. A new name was even introduced—altermagnet—to describe this class of magnets with zero net magnetization [31,44] [see Figs. 1(a)–1(c)]. Note that these centrosymmetric magnets

with zero magnetization and NRSS cannot be described by ferroic ordering of magnetoelectric multipoles, as this existence requires broken inversion symmetry.

We, therefore, pose the question of whether these altermagnetic AFMs are characterized by the ferroic ordering of a higher-order, parity-even magnetic multipole, analogous to the ferroic ordering of the parity-odd magnetoelectric multipoles in the magnetoelectric AFMs. A hint of such an ordering is already provided by the aspherical but centrosymmetric magnetization density probed in neutron scattering measurements [45] for the candidate *d*-wave NRSS material MnF_2 . Ferroically ordered magnetic multipoles would provide a natural explanation of the observed time-reversal symmetry breaking, in the same way that ferroic ordering of magnetic dipole moments breaks time-reversal symmetry in a ferromagnet, and would unify the various unconventional physical effects that are universal to this class of magnets. Furthermore, a description in terms of ferroic magnetic multipoles would help with identifying routes to controlling NRSS and magnetic domain orientations, both of which are crucial for possible device applications, thus expanding the potential utility of altermagnetic AFMs [46].

Here, we show that these time-reversal symmetry-broken, centrosymmetric AFMs with *d*-wave splitting, known as *d*-wave altermagnets, are conveniently described in terms of the ferroic ordering of magnetic octupoles. The magnetic octupoles form the next term in the magnetic multipole expansion after the magnetoelectric multipoles and are the lowest-order ferroically ordered magnetic quantity in this case. They are the natural order parameter for the transition into the magnetically ordered state and provide a convenient and unified description of the broken \mathcal{T} symmetry and the nonrelativistic spin splitting. They also account for other phenomena displayed by this class of antiferromagnets, such as the piezomagnetic effect [47,48] and strong magnetic anisotropy [49], and allow us to predict new behaviors such as an antipiezomagnetism. Finally, we show that, unusually for an antiferromagnet, magnetic octupoles lead to a nonzero magnetic Compton scattering, providing a route for their direct experimental detection.

We illustrate our ideas using rutile-structure manganese difluoride MnF_2 . MnF_2 has been widely explored as a classic example of a two-sublattice AFM over the past century [50–52] and was recently identified as a prototype centrosymmetric AFM with NRSS [26]. Importantly, Mn ions of opposite spin orientation have inequivalent fluorine environments [Fig. 1(d)]. This results in identical, ferroically ordered \mathcal{O}_{32^-} magnetic octupoles at each Mn site [Fig. 1(e)], which cause the broken \mathcal{T} symmetry in spite of the AFM spin compensation.

The remainder of the manuscript is organized as follows. We begin by briefly describing the crystal and magnetic structures of MnF_2 in Sec. II. This is followed by our discussion of the ordered magnetic octupoles in Sec. III.

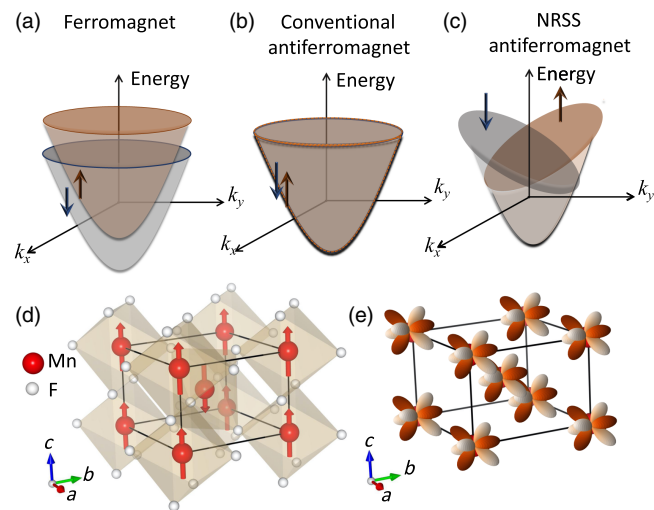


FIG. 1. NRSS antiferromagnets and ferrottype magnetic octupolar order. (a)–(c) show the spin splitting of the bands for conventional ferromagnets (Zeeman splitting), antiferromagnets (degenerate spin-polarized bands), and the recently discovered magnets with NRSS in the absence of net magnetization. (d) and (e) show the antiferrotype magnetic dipolar [arrows, (d)] order and ferrottype magnetic \mathcal{O}_{32^-} octupolar [colored anisotropic octupolar magnetic distribution, (e)] order in MnF_2 , respectively. The colored regions in (e) depict the angular distribution of the magnetization density corresponding to the \mathcal{O}_{32^-} octupole (see the text for details), where the red and white colors represent the regions of up and down spin polarization, respectively. As seen from the figure, the red and white regions of opposite spin polarization always appear in pairs, contributing thereby zero net magnetic moment.

In Sec. IV, we discuss the role of magnetic octupole in NRSS, predict new behaviors resulting from the ferromagneto-octupolar order that await experimental verification, and propose magnetic Compton scattering as a route to the direct detection of magnetic octupoles. Finally, we summarize our results and discuss promising future directions in Sec. V.

II. CRYSTAL AND MAGNETIC STRUCTURE

MnF₂ crystallizes in the centrosymmetric tetragonal rutile structure with the space-group symmetry $P4_2/mnm$ (D_{4h} point group) [26,53]. As depicted in Fig. 1(d), the unit cell contains two formula units, with two Mn atoms at the corner and the center of the unit cell, octahedrally coordinated by the F atoms. Importantly, the F environment around the Mn atom at the center is rotated by 90° around the z axis with respect to that at the corner Mn atom. As a result of this nonequivalent F environment, the Mn sites, although equivalent, are not related by a lattice translation. This has a crucial impact on the symmetry of the AFM structure of MnF₂ (magnetic space group $P4'_2/mnm'$) below the Néel temperature ($T_N = 67$ K [54]), where the collinear Mn spins align antiparallely along [001] [55] [see Fig. 1(d)]. Such a magnetic configuration breaks the \mathcal{T} symmetry despite the vanishing magnetization, since time reversal plus translation is not a symmetry of the antiferromagnetic configuration.

III. MAGNETIC OCTUPOLES IN MnF₂

The broken \mathcal{T} symmetry in the absence of any net magnetization is indicative of the existence of magnetic multipole of higher order than the magnetic dipole. Such multipoles appear in the expansion of the interaction energy \mathcal{E}_{int} between a spatially varying magnetic field $\vec{H}(\vec{r})$ and a magnetization density $\vec{\mu}(\vec{r})$ [9,56]:

$$\begin{aligned} \mathcal{E}_{\text{int}} &= - \int \vec{\mu}(\vec{r}) \cdot \vec{H}(\vec{r}) d^3 r \\ &= - \underbrace{\int \vec{\mu}(\vec{r}) \cdot \vec{H}(0) d^3 r}_{\text{dipolar term}} - \underbrace{\int r_i \mu_j(\vec{r}) \partial_i H_j(0) d^3 r}_{\text{magnetoelectric multipolar term}} \\ &\quad - \underbrace{\int r_i r_j \mu_k(\vec{r}) \partial_i \partial_j H_k(0) d^3 r}_{\text{octupolar term}} \dots \end{aligned} \quad (1)$$

In a compensated AFM, the net magnetization $\vec{M} = \int \vec{\mu}(\vec{r}) d^3 r$ is absent, and so the conventional dipolar Zeeman term, which is the first term in the above expansion, does not contribute. Furthermore, the presence of inversion symmetry in centrosymmetric antiferromagnets with NRSS forbids the existence of any ferrotype magnetoelectric multipole $\mathcal{M}_{ij} = \int r_i \mu_j(\vec{r}) d^3 r$, since these break inversion symmetry, forming the second term in

Eq. (1). This makes the first symmetry-allowed ferrotype magnetic multipole the inversion-symmetric rank-3 magnetic octupole $\mathcal{O}_{ijk} = \int r_i r_j \mu_k(\vec{r}) d^3 r$, which forms the third term in the above expansion. While this simple symmetry argument suggests that the magnetic octupole is the first allowed net nonzero magnetic multipole in a centrosymmetric AFM with NRSS, its existence can be confirmed only through an explicit computational analysis of the multipoles.

In the following, we take MnF₂ as a representative system for such unconventional AFMs with d -wave splitting and explicitly analyze the multipoles in the system. In particular, we focus on the magnetic octupole and show its possible manipulation via structural and magnetic modifications.

A. Multipole analysis

In order to identify the relative arrangement of magnetic octupoles between the Mn atoms, we compute the multipoles within an atomic sphere around each atom, known as the atomic-site multipoles, in the bulk, periodic solid. For this, we decompose the density matrix $\rho_{l_1 m_1, l_2 m_2}$, computed using density-functional theory (DFT) as implemented in the ELK code (see the computational details in Appendix A), into tensor moments centered at each atomic site [9,57]. These atomic-site multipoles offer a microscopic representation of the existence and ordering of multipoles at each atomic site [58] and complement other approaches, such as the local moment [59,60] and cluster multipoles approaches [61–64]. The local moment approach describes the multipoles resulting from the asymmetric arrangement of local magnetic dipole moments at each magnetic site within the unit cell. On the other hand, in the cluster multipole approach, the magnetic configuration, corresponding to symmetry-adapted multipole moments, is initially defined within a “virtual” atomic cluster of the target crystal and subsequently mapped onto the crystal while preserving the magnetic point group of the multipole moments.

In the present work, for the computation of atomic-site multipoles, since the desired parity-even multipoles (as the structure has inversion symmetry) have contributions from even $l_1 + l_2$ terms, we evaluate both $d-d$ and $p-p$ matrix element contributions. We consider both \mathcal{T} -even (charge) and -odd (magnetic) multipoles.

We now analyze the computed irreducible (IR) components of the rank-3 magnetic octupole \mathcal{O}_{ijk} tensor in the multipole expansion of Eq. (1). The details of these IR components are discussed later in Sec. IV B and given in Appendix B. We represent the elements of the totally symmetric traceless part of the \mathcal{O}_{ijk} tensor by \mathcal{O}_{lm} , where the indices $l = 3$ with components $m = -3, -2, \dots, 2, 3$ represent the spherical harmonics that are used to build these tensors [65]. The only nonzero \mathcal{O}_{lm} in MnF₂ are \mathcal{O}_{32} - and \mathcal{O}_{30} . Similarly, among the charge quadrupole moment components \mathcal{Q}_{lm} , with $l = 2$ and $m = -2, -1, \dots, 1, 2$, the

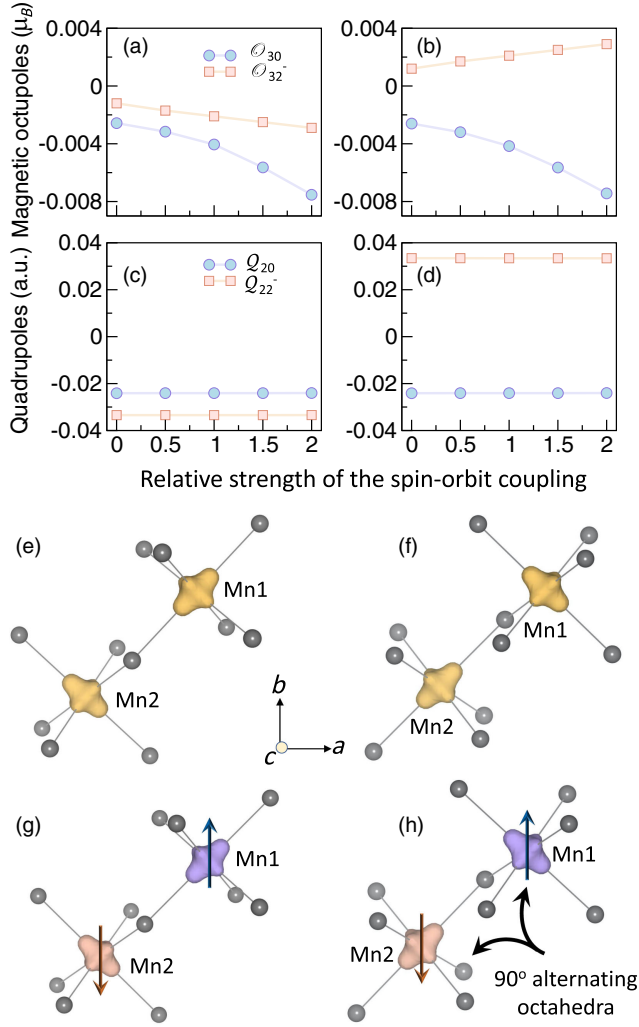


FIG. 2. Variation of magnetic octupoles at the Mn atoms as the relative strength of the spin-orbit coupling λ_r is varied for the (a) crystal structure of MnF_2 and (b) modified structure. The same variation of the charge quadrupoles for the (c) crystal structure of MnF_2 and (d) modified structure. Here, $\lambda_r = \lambda_f/\lambda$, with λ_f and λ being the enforced value of the spin-orbit coupling constant in the calculation and its actual value in the material, respectively. The band-decomposed charge densities for the top valence band in Fig. 4(a) of MnF_2 in the $a-b$ plane for the (e) crystal structure of MnF_2 and (f) modified structure. (g) and (h) are the same, showing the band-decomposed magnetization densities. The up and down arrows in (g) and (h) indicate the up and down spin magnetic dipole moment, respectively, with the polarization axis along \hat{z} . The opposite MnF_6 octahedral rotations are indicated in black arrows.

charge quadrupole moments Q_{22^-} and Q_{20} have nonzero values in MnF_2 . The computed values of the magnetic octupoles, O_{32^-} and O_{30} , and charge quadrupoles, Q_{22^-} and Q_{20} , are shown in Figs. 2(a) and 2(c) as the relative strength of the spin-orbit coupling (SOC) constant λ_r is varied. As we can see from this variation, the magnetic octupoles are nonzero even without the presence of the spin-orbit

coupling. This indicates that the magnetic octupole in MnF_2 is of nonrelativistic origin in contrast to the spin-orbit coupled higher-order magnetic multipoles in heavy fermion systems [57,66–68]. Consequently, in contrast to the symmetry breaking in the spin-orbit coupled J states of the f shell, the time-reversal symmetry breaking in this case causes a pure spin splitting, as we discuss later in Sec. IV A. It is also clear from Fig. 2(a) that the magnitudes of the magnetic octupoles depend on λ_r , whereas the values of the quadrupoles remain invariant, suggesting that the quadrupoles have only structural origin while the magnetic octupoles may have both structural and magnetic dependencies. The dependence of both magnetic octupoles on the strength of the spin-orbit coupling is, however, very weak; for example, the change in the value of the O_{32^-} octupole (ΔO_{32^-}) due to the change in the relative strength of the spin-orbit coupling $\Delta\lambda_r$, i.e., $\Delta O_{32^-}/\Delta\lambda_r$, is only 0.08%. Also, a pure structural origin of quadrupoles is not a general case for any systems with quadrupolar distortion; e.g., the quadrupoles in the iso-space-group compound $\text{Ba}_2\text{MgReO}_6$ (with a canted antiferromagnetic spin configuration) are reported to have a strong spin dependence [69].

The computed magnetic multipoles show the presence of a ferrottype magnetic octupole O_{32^-} [Fig. 1(e)] with real-space representation xym_z (where m_z is the z component of the magnetic moment) at the Mn sites, belonging to the totally symmetric IR representation A_{1g} of the D_{4h} point group symmetry (see the character table in Appendix C) of the crystal structure. The existence of the magnetic octupole is also consistent with the B_{1g}^- active representation (see Appendix C) of MnF_2 and the symmetry analysis described earlier.

The magnetic octupoles O_{30} with real-space representation $(3z^2 - r^2)m_z$ also have a nonzero value at the Mn sites; however, they have antiparallel alignment between the Mn sites, resulting in an absence of net O_{30} octupole moment. Among the other IR components of the O_{ijk} tensor, we also found nonzero magnetic octupole components $Q_{x^2-y^2}^{(\tau)}$ and $t_z^{(\tau)}$ with ferro- and antiferrottype alignments, respectively. These are also known as the magnetic toroidal quadrupole moment ($Q_{ij}^{(\tau)}$) and moment of the magnetic toroidal multipole ($t_i^{(\tau)}$), respectively, and are parts of the non-symmetric IR components of the full O_{ijk} tensor (see Appendix B). Thus, the full O_{ijk} tensor in the magnetic multipole expansion in Eq. (1) contains both magnetic and magnetic toroidal multipoles, unlike the cluster multipolar approach [61–64], which uses two separate expansions for the magnetic and magnetic toroidal multipoles. Consequently, the $Q_{ij}^{(\tau)}$ and $t_i^{(\tau)}$ terms naturally appear in the same order as the totally symmetric traceless components O_{lm} in the same magnetic multipole expansion. We discuss the IR components of the octupole tensor later in

detail in Sec. IV B. In addition to these magnetic octupoles, the crystal structure of MnF_2 also hosts charge quadrupoles, Q_{20} with $(3z^2 - r^2)$ distortion and Q_{22^-} , representing the xy -structural distortion, which have ferro- and antiferrotype alignments, respectively.

For a physical understanding and better visualization, we further compute the band-decomposed charge and spin densities for the top valence band (which also undergoes NRSS) in the electronic structure of MnF_2 , shown in Fig. 4(a), and the results are shown in Figs. 2(e) and 2(g). As apparent from the figure, the charge density around the Mn atoms is highly anisotropic in the x - y plane, a signature of the existing Q_{22^-} quadrupole. Interestingly, the spin density around the Mn atoms, shown in Fig. 2(g), follows the anisotropic charge density, indicating a correlation between the spin anisotropy (quantified by the magnetic octupoles) and the charge anisotropy (quantified by the charge quadrupoles). This further justifies the weak dependence of the octupoles on λ_r .

Furthermore, to examine the effect of the Hubbard U , we compute the magnetic octupoles O_{32^-} and O_{30} and the charge quadrupoles Q_{22^-} and Q_{20} for a range of values of the U parameter. The results of our calculations are depicted in Figs. 3(a) and 3(b). As seen from these plots,

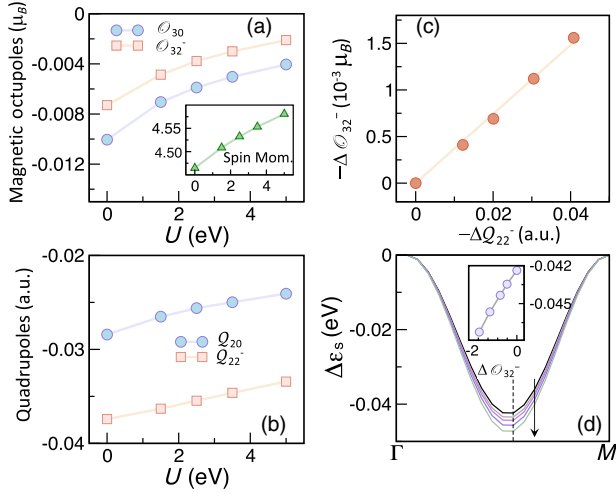


FIG. 3. Variation of (a) magnetic octupoles and (b) charge quadrupoles for each Mn ion as a function of Hubbard U . The inset shows the same variation for the spin magnetic dipole moment for each Mn ion in μ_B . (c) Variation of the difference in the magnetic octupole moment O_{32^-} , $\Delta O_{32^-} = O_{32^-}^c - O_{32^-}^a$, as the difference in the charge quadrupole moment Q_{22^-} , $\Delta Q_{22^-} = Q_{22^-}^c - Q_{22^-}^a$, increases. Here, $Q_{22^-}^c$ and $O_{32^-}^c$ are the constrained quadrupole moment and the resulting magnetic octupole moment, respectively, while $Q_{22^-}^a$ and $O_{32^-}^a$ are the same for the actual crystal structure without any constrained moment. (d) The variation of the energy difference $\Delta \epsilon_s$ between the spin-split top two valence bands shown in Fig. 4(a) along $\Gamma \rightarrow M$ as ΔO_{32^-} increases. The arrow indicates the increasing absolute value of ΔO_{32^-} from 0 to 2 as depicted in the inset. The inset shows the variation of $\Delta \epsilon_s$ at the k point indicated by the vertical line in the main plot for different values of ΔO_{32^-} .

the magnitudes of both magnetic octupole and the charge quadrupole moments decrease with an increase in U . The similar variation of the quadrupole and the octupole moments further confirms the dependencies of magnetic octupole on the structural distortion, quantified by the charge quadrupole moment. We note that, although with an increase in U the spin dipole moment increases in magnitude [see the inset in Fig. 3(a)] as expected, the magnetic octupole moments decrease in magnitude, confirming that the atomic-site magnetic octupole moment is not biased by the magnetic dipole moment.

B. Magnetic octupolar domains: Correlation to structure and spin

We now show how the coupling between magnetic octupoles and charge quadrupoles determines the magnetic octupolar domains. Since the magnetic octupoles are linked to the NRSS, as we show in the next section, the understanding of the magnetic octupolar domain is also useful in manipulating the NRSS.

We begin by changing the fluorine environment around the Mn atoms, without affecting the spin arrangements at the Mn sites. Specifically, we change the coordinates of the F ions from $4f: (x, x, 0) \rightarrow 4g: (x, -x, 0)$, which alters the F-Wyckoff site symmetry from $4f$ to $4g$, while keeping the space-group symmetry unchanged. We note that structurally (without considering the magnetism), the new structure is equivalent to the original crystal structure of MnF_2 [shown in Fig. 1(c)], with a shifted origin at $(0.5, 0.5, 0.5)$, so that the central and corner Mn atoms are exchanged in the new structure. This results in a 90° alternation of MnF_6 octahedral rotation and, hence, their distortion in the x - y plane [see Figs. 2(e)–2(h)]. Correspondingly, this leads to a reversal of sign in the computed antiferrotype Q_{22^-} quadrupole for the modified structure, as depicted in Fig. 2(d). This is also evident from the changes in the anisotropic charge density distribution around the Mn atoms in the modified structure as shown in Fig. 2(f). Note that the modified fluorine environment, however, does not affect the distortion of the MnF_6 octahedra along z direction, and the sign of the ferrotype Q_{20} quadrupole, therefore, remains unaltered [see Fig. 2(d)].

In order to see the impact of the charge quadrupoles on the magnetic octupoles, we further analyze the magnetic multipoles of this modified structure. Interestingly, our computed octupoles show that the sign of the O_{32^-} octupole reverses whereas that of O_{30} remains as it is [see Fig. 2(b)], showing the reversal of the magnetic octupolar domain. Corresponding changes in the anisotropic magnetization density around the Mn atoms are shown in Fig. 2(h). This also emphasizes the correlation between O_{32^-} octupole and Q_{22^-} quadrupole—and O_{30} octupole and Q_{20} quadrupole. Note that the O_{32^-} and O_{30} octupoles remain ferro- and antiferrotype, respectively. This suggests selecting the magnetic octupolar domain by changing only the position

of the nonmagnetic F atoms, without affecting the magnetic Mn atom's position or its spin arrangements, emphasizing a strong interplay between lattice and the magnetic configuration, quantified by the magnetic octupole.

We note that the dependence of the surrounding nonmagnetic atoms on the magnetic anisotropy, as discussed above, is consistent with the discussion in Ref. [22]. The advantage of the present multipolar formalism, however, is that it provides a quantification for the surrounding nonmagnetic environment. Such a quantification is particularly desirable in understanding how to control the magnetic anisotropy dictated by the magnetic octupoles. While the dependence of the sign of the magnetic octupole \mathcal{O}_{32^-} on that of the charge quadrupole \mathcal{Q}_{22^-} is apparent from our previous analysis, for a systematic control of the magnetic octupole, it is also important to confirm the dependence of the strength of the magnetic octupole \mathcal{O}_{32^-} on the charge quadrupole \mathcal{Q}_{22^-} .

For this purpose, we constrain the value of the charge quadrupole moment \mathcal{Q}_{22^-} in our calculation, keeping the crystal structure and the magnetic configuration unaltered (see Appendix A for the computational details). The results of our calculation are shown in Fig. 3(c), where the resulting change in the value of magnetic octupole moment $\Delta\mathcal{O}_{32^-} = \mathcal{O}_{32^-}^c - \mathcal{O}_{32^-}^a$ with respect to its value $\mathcal{O}_{32^-}^a$ in the actual crystal structure is shown as a function of the excess quadrupole moment $\Delta\mathcal{Q}_{22^-} = \mathcal{Q}_{22^-}^c - \mathcal{Q}_{22^-}^a$. Here, $\mathcal{Q}_{22^-}^c$ and $\mathcal{O}_{32^-}^c$ are the constrained quadrupole moment and the resulting magnetic octupole moment, respectively. Note that the zero values in $\Delta\mathcal{Q}_{22^-}$ and $\Delta\mathcal{O}_{32^-}$ in Fig. 3(c) correspond to the actual crystal structure (without any constrained moment) with their ground state nonzero values $\mathcal{Q}_{22^-}^a$ and $\mathcal{O}_{32^-}^a$ of the charge quadrupole and magnetic octupole moments, respectively. As visible from Fig. 3(c), an increase in the magnitude of the charge quadrupole moment also increases the magnitude of the magnetic octupole moment, suggesting that not only the sign, but also the magnitude of the magnetic octupole moment \mathcal{O}_{32^-} can be systematically controlled by manipulating the charge quadrupole moment \mathcal{Q}_{22^-} . This, in turn, also provides a way to manipulate the nonrelativistic spin splitting, which we discuss later in Sec. IV A.

We close this section by describing the manipulation of the magnetic octupole by flipping the direction of all the Mn spins while keeping the same antiferromagnetic arrangement between the Mn atoms. Physically, it corresponds to a different antiferromagnetic domain. The reversal of the Mn spins results in a reversal of the sign of both octupoles, in contrast to the previous case where only the ferrottype \mathcal{O}_{32^-} octupole reverses its sign. Note that in this case charge quadrupoles remain the same, as they do not depend on the spin arrangement.

It is interesting to point out that this manipulation of the magnetic octupole has, in fact, important physical implications. For example, the two antiferromagnetic domains

with ferrottype octupoles of opposite sign can also be visualized as two separate ferro-octupolar domains. Such revisualization is particularly useful in describing important physical properties that are characteristics of the magnetic octupoles as well as understanding the conjugate fields for creating such ferro-octupolar domains. Since the free energy remains invariant under both space inversion and time reversal, the conjugate field for the magnetic octupole, which must have the same symmetry as the magnetic octupole, should also be even under space inversion and odd under time reversal. This suggests that the product of the shear stress and the magnetic field is a valid choice for the conjugate field of the magnetic octupole, which can, therefore, be used to select a particular magnetic domain, as we also discuss later in Sec. IV.

IV. IMPLICATIONS OF MAGNETIC OCTUPOLE

Next, we discuss the implications of the existence of the magnetic octupole, including its role in the NRSS as well as other unconventional physical properties that, in turn, can be used for its possible direct measurements. This section is ordered as follows: (A) the relevance to NRSS, (B) the resulting piezo- and antipiezomagnetic effects, and (C) the possible detection of magnetic octupoles using the magnetic Compton scattering effect. Once again, we take MnF_2 as our example material for illustration. We show that the existence of the ferrottype magnetic octupole \mathcal{O}_{32^-} both conveniently describes the NRSS and provides a way to manipulate it. Then, we show that the ferromagneto octupolar ordering is responsible for the well-known piezomagnetic effect in MnF_2 . More interestingly, our identification of the antiferrottype magnetic octupoles allows us to predict a previously unknown antipiezomagnetic effect. In addition to the underlying fundamental physics and technological applications of these effects, we also propose magnetic Compton scattering as an experimental technique for the detection of the apparently *hidden* magnetic octupoles. The corresponding measurement setup as guidance for future experiments is also discussed.

A. Relevance to nonrelativistic spin splitting

We link the unconventional spin splitting of the energy bands in the Brillouin zone (BZ) of the antiferromagnetic MnF_2 to the ferro-octupolar order using the reciprocal-space representation of the ferrottype octupole. Since the magnetic octupole can be manipulated by modifying the F-environment or the spin arrangements, as discussed above, we show that these changes can also be used to manipulate the spin splitting of the bands.

Our calculated antiferromagnetic band structure of MnF_2 in both the presence and absence of spin-orbit interaction is depicted in Fig. 4(a). As we see from the band structure, there is a significant energy splitting between the up and down spin bands along the $\Gamma \rightarrow M$ direction in the BZ of

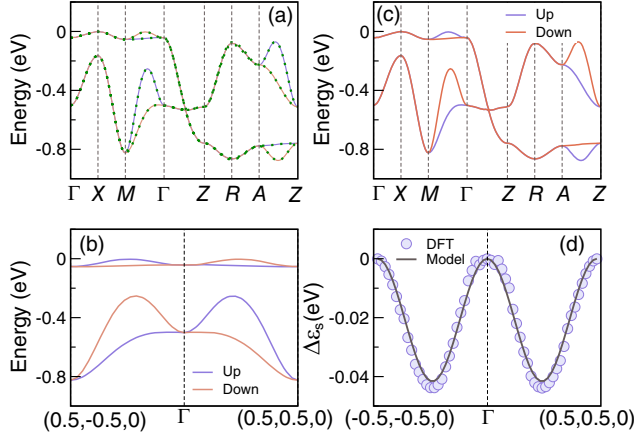


FIG. 4. Spin splitting in MnF_2 . (a) Band structure of MnF_2 in both the absence and presence of spin-orbit interaction, depicting the spin splitting along the $M \rightarrow \Gamma$ direction. The up and down spin-polarized bands in the absence of spin-orbit coupling are shown in solid blue and red lines, respectively, and the bands in the presence of spin-orbit interaction are indicated in green dots. (b) The corresponding band structure along the same high-symmetry k path for the hypothetical modified structure (see the text for details), showing the reversal of spin splitting along $M \rightarrow \Gamma$. (c) Band structure of MnF_2 showing the reversal of spin splitting as the momentum direction changes from $[1\bar{1}0]$ to $[110]$. (d) A comparison of the DFT result and the tight-binding analytical expression, Eq. (6), for the energy splitting between the two top-most spin-polarized bands in (a).

MnF_2 . Interestingly, the splitting is present even without the spin-orbit interaction, and inclusion of spin-orbit interaction does not affect the energy splitting along that direction, in agreement with the reported band structure in Ref. [26]. The splitting is large compared to the typical relativistic Rashba-type spin splitting and does not require any broken inversion symmetry of the structure [70].

To understand this unconventional spin splitting in MnF_2 , we analyze the reciprocal-space representation of the ferrotypic \mathcal{O}_{32^-} octupole. The reciprocal space representations of the multipoles have been used successfully to describe the band asymmetries in the BZ of noncentrosymmetric materials [13,71,72]. In contrast to the odd-parity multipoles, for which the real and reciprocal-space representations are rather counterintuitive, for the even-parity multipoles, such as the \mathcal{O}_{32^-} magnetic octupole, that are relevant here, the analysis is much more straightforward. The reciprocal-space representation in this case can simply be obtained by replacing $\vec{r} \rightarrow \vec{k}$ so that the reciprocal-space representation of \mathcal{O}_{32^-} octupole (xym_z in real space) is $k_x k_y m_z$. This immediately explains the splitting between up and down spin-polarized bands, with the spin polarization along \hat{z} (i.e., with spin moment m_z), along the $[110]$ direction in the momentum space, e.g., $\Gamma \rightarrow M$ and $A \rightarrow Z$ directions in momentum space. Note that such splitting will occur along any momentum direction with nonzero k_x and k_y .

Interestingly, since the reciprocal-space representation is an even function of \vec{k} , the resulting spin splitting should also be symmetric, in contrast to the antisymmetric spin splitting in the Rashba interaction. This indeed is the case, e.g., in MnF_2 with identical spin splitting along the $[110]$ and $[\bar{1}\bar{1}0]$ directions in momentum space. In addition, from the representation $k_x k_y m_z$, we also expect the spin splitting to reverse as the direction in the momentum space changes from $[110]$ to $[1\bar{1}0]$ (d -wave spin splitting). Indeed, the computed DFT band structure depicts such reversal of spin splitting under \mathcal{C}_4 rotation of the momentum direction, as shown in Fig. 4(b). The representation analysis, therefore, confirms that the ferrotypic ordering of the \mathcal{O}_{32^-} octupoles is responsible for the spin splitting of the energy bands, analogous to the spin splitting of bands in a conventional ferromagnet with ferrotypic magnetic dipole.

Note that the atomic-site magnetic octupole, discussed here, is distinct from the cluster and bond multipoles, proposed by Hayami, Yanagi, and Kusunose [25,73] to describe spin splitting in collinear antiferromagnets. The magnetic octupole description has the advantage that it naturally occurs in a magnetic multipole expansion, correctly captures the magnetic anisotropy at the atomic scale without any bias toward particular combinations of the magnetic dipole moments, and also describes the order parameter for such unconventional antiferromagnetism, as discussed above. The rank-3 magnetic octupole is also distinct from the anisotropic magnetic dipole predicted in Ref. [74], which is a rank-1 tensor.

To further verify the role of \mathcal{O}_{32^-} octupole in generating the spin splitting, we analyze the spin splitting of the bands for the case of structural modification, discussed in the previous section, for which the \mathcal{O}_{32^-} octupole switches sign. As expected, in this case, the spin splitting also reverses [see Fig. 4(c)]. Similar reversal of the spin splitting also occurs for the opposite magnetic dipolar domain (not shown here), in which the magnetic \mathcal{O}_{32^-} octupole also switches sign.

To understand the dependence of the amount of spin splitting as the magnitude of the magnetic octupole moment \mathcal{O}_{32^-} varies, we analyze the band structure for different values of magnetic octupole moment \mathcal{O}_{32^-} that we obtain by tuning the value of the charge quadrupole moment \mathcal{Q}_{22^-} , as discussed in the previous section and also depicted in Fig. 3(c). The energy difference $\Delta\mathcal{E}_s$ between the topmost spin-split valence bands in Fig. 4(a) along the $\Gamma \rightarrow M$ direction is shown in Fig. 3(d) for these different values of the magnetic octupole moments \mathcal{O}_{32^-} . As evident from this figure, the magnitude of $\Delta\mathcal{E}_s$ increases as the \mathcal{O}_{32^-} octupole moment increases (indicated by the direction of the arrow). The value of $\Delta\mathcal{E}_s$ at a specific k point, indicated by the vertical line in Fig. 3(d), is explicitly shown in the inset for the different values of $\Delta\mathcal{O}_{32^-}$, confirming the direct dependence of the amount of spin splitting on the strength of the magnetic octupole \mathcal{O}_{32^-} . This further implies a

systematic control of the nonrelativistic spin splitting by manipulating the magnetic octupole moment \mathcal{O}_{32^-} . It is important to point out that, in general, magnetic octupoles can occur without causing NRSS, if they are induced by spin-orbit interaction. In g - and i -wave altermagnets, for example, only SOC-induced octupoles can be present and the NRSS is related to higher-order multipoles as we discuss later. However, their existence in a collinear AFM in the absence of the spin-orbit interaction always leads to NRSS in the momentum space.

1. Role of microscopic parameters in the spin splitting

Having shown that the ferrotype ordering of the magnetic octupoles generates the spin splitting in MnF_2 , to determine the role of different microscopic parameters, such as electronic hopping, exchange splitting, etc., on the strength of the spin splitting, we next carry out a low-energy tight-binding (TB) analysis. For this purpose, we construct a minimal four-band TB model in the Bloch function basis with the order of the basis set in the sequence $\{\text{Mn1} - d_{xz}, \text{Mn1} - d_{yz}, \text{Mn2} - d_{xz}, \text{Mn2} - d_{yz}\}$. The Hamiltonian reads as follows:

$$\begin{aligned} \mathcal{H}_t = & \alpha(\vec{k})\mathbb{I} + \beta(\vec{k})\vec{\Sigma}_z \otimes \sigma_x + \gamma(\vec{k})\vec{\Sigma}_x \otimes \sigma_0 \\ & + \delta(\vec{k})\vec{\Sigma}_x \otimes \sigma_x. \end{aligned} \quad (2)$$

Here, \mathbb{I} is a 4×4 identity matrix, $\vec{\Sigma}$ and $\vec{\sigma}$ are the Pauli matrices in the sublattice bases of Mn1 and Mn2 and in the orbital bases of d_{xz} and d_{yz} , respectively, and σ_0 is an identity matrix in the orbital bases. The choice of the orbitals is governed by the predominant orbital characters of the top pair of valence bands along $\Gamma \rightarrow M$ in the BZ of MnF_2 (see Fig. 7 in Appendix D). The functions $\alpha(\vec{k})$, $\beta(\vec{k})$, $\gamma(\vec{k})$, and $\delta(\vec{k})$ are determined by the effective $d-d$ hopping parameters (t_i , $i = 1, 4$) and the on-site energies (ϵ_i , $i = 1, 2$) of the orbitals, and their explicit functional forms are given below:

$$\begin{aligned} \alpha(\vec{k}) &= \epsilon_1 + 2t_1 \cos(k_z c), \\ \beta(\vec{k}) &= \epsilon_2 + 2t_2 \cos(k_z c), \\ \gamma(\vec{k}) &= 8t_3 \cos\left(\frac{k_x a}{2}\right) \cos\left(\frac{k_y a}{2}\right) \cos\left(\frac{k_z c}{2}\right), \\ \delta(\vec{k}) &= -8t_4 \sin\left(\frac{k_x a}{2}\right) \sin\left(\frac{k_y a}{2}\right) \cos\left(\frac{k_z c}{2}\right). \end{aligned} \quad (3)$$

Here, a and c are the lattice constants of the tetragonal structure. For simplicity, we consider electronic hoppings only up to second nearest neighbor, and the realistic TB parameters are extracted from the DFT band structure of MnF_2 using the N th-order muffin-tin orbital (NMTO) downfolding technique [75].

The diagonalization of the Hamiltonian in Eq. (2) gives us the four energy eigenvalues:

$$\begin{aligned} \mathcal{E}_\pm^-(\vec{k}) &= \alpha(\vec{k}) - \{\beta(\vec{k})^2 + [\delta(\vec{k}) \pm \gamma(\vec{k})]^2\}^{1/2} \\ \mathcal{E}_\pm^+(\vec{k}) &= \alpha(\vec{k}) + \{\beta(\vec{k})^2 + [\delta(\vec{k}) \pm \gamma(\vec{k})]^2\}^{1/2}. \end{aligned} \quad (4)$$

Analysis of the corresponding eigenvectors shows that there is an energy splitting $\Delta\mathcal{E} = \mathcal{E}_+^-(\vec{k}) - \mathcal{E}_-^-(\vec{k})$ between bands of dominant Mn1 and Mn2 sublattice contributions. Note that such energy splitting between bands of different sublattice characters is present prior to including the effect of antiferromagnet exchange splitting J . We now show that the inclusion of J translates the sublattice splitting of the bands into the spin splitting of the bands.

To include the effect of the antiferromagnetic exchange, we rewrite the Hamiltonian (2) in the basis of $\{\text{Mn1} - d_{xz}\uparrow, \text{Mn1} - d_{yz}\uparrow, \text{Mn2} - d_{xz}\uparrow, \text{Mn2} - d_{yz}\uparrow, \text{Mn1} - d_{xz}\downarrow, \text{Mn1} - d_{yz}\downarrow, \text{Mn2} - d_{xz}\downarrow, \text{Mn2} - d_{yz}\downarrow\}$ and add the exchange term $\mathcal{H}_{\text{ex}}^{\text{AFM}} = JS_z \otimes (\Sigma_z \otimes \sigma_0)$ to it. The full Hamiltonian is given by

$$\mathcal{H} = S_0 \otimes \mathcal{H}_t + JS_z \otimes (\Sigma_z \otimes \sigma_0). \quad (5)$$

Here, \vec{S} and S_0 are the Pauli matrices and the identity matrix in the spin basis, respectively. The exchange splitting energy between up and down spin-polarized bands, $2J \approx 5$ eV, is extracted from the computed spin-polarized densities of states of MnF_2 .

By diagonalizing the Hamiltonian (5), we obtain the energy eigenvalues and focus on the spin-polarized topmost valence bands, with energies \mathcal{E}_\uparrow and \mathcal{E}_\downarrow . We note that their eigenvalues are identical to those of \mathcal{E}_\pm^{\pm} in Eq. (4), except that $\beta(\vec{k}) \rightarrow J + \beta(\vec{k})$. Physically, this means that the two Mn sublattices, that primarily contribute to those bands, have opposite spin polarization in the presence of antiferromagnetism, and, therefore, they lead to the spin splitting of the bands. The explicit analytical form of the energy splitting is given by

$$\begin{aligned} \Delta\mathcal{E}_s &= \mathcal{E}_\uparrow - \mathcal{E}_\downarrow \\ &= \{(J + \beta)^2 + (\delta - \gamma)^2\}^{1/2} - \{(\beta + J)^2 + (\delta + \gamma)^2\}^{1/2} \\ &\approx \frac{32}{\epsilon} t_3 t_4 \sin(k_x a) \sin(k_y a). \end{aligned} \quad (6)$$

Here, in obtaining the last equality we use the fact that $\epsilon \gg (\delta + \gamma)$, where $\epsilon = J + \beta \approx J + \epsilon_2 + 2t_2$, using Eq. (3) and ignoring terms that are second order in k_z or higher. Note that this approximation in ϵ becomes exact in the $k_z = 0$ plane, which contains the desired $\Gamma \rightarrow M$ momentum direction of spin splitting. For a realistic set of parameters (listed in Appendix E), we compare the analytical result in Eq. (6) to the DFT computed energy splitting of the spin-polarized bands. As depicted in

Fig. 4(d), they agree reasonably with each other, suggesting that our minimal model captures the essential physics of the spin splitting in MnF_2 .

We pause here and analyze the obtained analytical relation in Eq. (6) for the spin-splitting energy. First of all, it is clear from Eq. (6) that $\Delta\mathcal{E}_s(\vec{k}) = \Delta\mathcal{E}_s(-\vec{k})$; i.e., it is symmetric in \vec{k} but changes sign under $(k_x, k_y) \rightarrow (k_x, -k_y)$, consistent with the computed DFT bands. Second, we see that the splitting energy $\Delta\mathcal{E}_s$ depends directly on the intersublattice hopping parameters t_3 (intraorbital) and t_4 (interorbital), in the absence of which $\Delta\mathcal{E}_s$ vanishes. This emphasizes the crucial role of interaction between the two sublattices, which, in combination with the antiferromagnetic exchange, generates the spin splitting. Physically, this indicates that a structure-spin correlation, a reminiscent of the magnetic octupole as discussed before, is responsible for the spin splitting. It is interesting to point out that the intersublattice hopping t_4 (as well as the product t_3t_4) in MnF_2 is a symmetric hopping, and it changes sign as the direction of hopping changes from $[11z]$ to $[1\bar{1}z]$ with $z \neq 0$ leading to symmetric spin splitting. This is analogous to the antisymmetric hopping in a nonmagnetic broken-inversion symmetric system that gives rise to Rashba-like antisymmetric spin splitting of the energy bands [72].

Finally, the TB analysis also provides a microscopic understanding of the reversal of spin splitting described before. For the modified structure, the on-site energy ε_2 and the hopping t_2 change sign, leading to a sign change in β . While the sign change does not affect the energy eigenvalues $\mathcal{E}_\pm(\vec{k})$ in Eq. (4) (since the dependence on β comes in even power), it reverses the dominant sublattice contributions in the corresponding eigenvectors (as also evident from the full DFT band structure, depicted in Appendix D), resulting in a reversal of sublattice splitting of bands. Since the sublattice splitting later transforms into the spin splitting, this consequently leads to the reversal of the spin splitting. The reversal of spin splitting for the other antiferromagnetic domain follows directly from the resulting sign change in the antiferromagnetic exchange J , which, in turn, alters the spin polarization of the bands.

Overall, the TB analysis provides a crucial insight into the roles of different microscopic parameters in generating the unconventional spin splitting of the energy bands in MnF_2 . The TB analysis further serves as a link between the proposed ‘‘modern’’ ferro-octupolar order and the conventional antiferromagnetic dipolar order.

B. Piezo- and antipiezomagnetic effects

The piezomagnetic effect describes changes in magnetization due to an applied stress or changes in shape due to an applied magnetic field. It is particularly promising for applications, because it provides a means for manipulating magnetism via strain engineering in antiferromagnets. In addition, since it is a linear coupling in contrast to

the quadratic coupling in the commonly used magnetostriction, it also allows for magnetization switching. The recent demonstration that the dynamically excited optical phonons can induce the symmetry-breaking lattice distortions required in the piezomagnetic effect [76–78] has revived interest. Such optically induced strain would overcome the limitation of a large mechanical strain and lead to practical applications in memory and spintronic devices.

The piezomagnetic effect has been predicted and experimentally shown for some AFMs with NRSS [47,48,76]. In this section, we show that the piezomagnetic effect is the result of ferroic ordering of magnetic octupoles and illustrate our ideas for the specific example of MnF_2 . In addition, we predict an antipiezomagnetic effect in MnF_2 resulting from the antiferrotype \mathcal{O}_{30} magnetic octupole.

1. General symmetry description

We begin by correlating the symmetries of the magnetic octupole and the piezomagnetic response. We note that both are rank-3 tensors and have the same symmetry, breaking time-reversal symmetry while keeping inversion symmetry intact. To correlate the elements of the piezomagnetic response to the magnetic octupole, we analyze the nonzero elements in the magnetic octupole tensor $\mathcal{O}_{ijk} = \int \mu_i r_j r_k d^3r$ following the tensor decomposition reported in Ref. [65]. Note that, in general, i, j , and k are the dummy indices, and to be consistent with the indices of the piezomagnetic response tensor Λ_{ijk} , here, we associate the index i to the magnetization and j and k to spatial coordinates so that the octupole \mathcal{O}_{ijk} is symmetric under the exchange of j and k indices by construction.

The octupole \mathcal{O}_{ijk} can be decomposed into a totally symmetric tensor \mathcal{S}_{ijk} of dimension 10 and an eight-dimensional nonsymmetric residue tensor \mathcal{R}_{ijk} that account for the 18 independent elements of \mathcal{O}_{ijk} [65]. The totally symmetric tensor \mathcal{S}_{ijk} can be further decomposed into a traceless totally symmetric part $\tilde{\mathcal{S}}_{ijk}$ and a trace part \mathcal{T}_{ijk} of dimensions 7 and 3, respectively, and the residue tensor \mathcal{R}_{ijk} into two irreducible components $\tilde{\mathcal{R}}_{ijk}^{(5)}$ and $\tilde{\mathcal{R}}_{ijk}^{(3)}$ of dimensions 5 and 3, respectively, so that $\mathcal{O}_{ijk} = \tilde{\mathcal{S}}_{ijk} + \mathcal{T}_{ijk} + \tilde{\mathcal{R}}_{ijk}^{(5)} + \tilde{\mathcal{R}}_{ijk}^{(3)}$. The explicit forms of each of these irreducible components are given in Appendix B. Note that the seven independent components of the totally symmetric traceless part $\tilde{\mathcal{S}}_{ijk}$ can be built from the spherical harmonics with $l = 3$, and, hence, these components are often exclusively referred to as the magnetic octupole, in contrast to the entire \mathcal{O}_{ijk} tensor.

We now explicitly consider the case of MnF_2 , which is known to exhibit a piezomagnetic effect [47,79–81] with the nonzero elements of the piezomagnetic response tensor Λ_{ijk} , $\Lambda_{xyz} = \Lambda_{yxz} \neq \Lambda_{zxy}$ so that

$$\mathcal{M}_x = \Lambda_{xyz}\sigma_{yz}, \quad \mathcal{M}_y = \Lambda_{yxz}\sigma_{xz}, \quad \mathcal{M}_z = \Lambda_{zxy}\sigma_{xy}, \quad (7)$$

where \vec{M} is the magnetization that results from the application of shear stress σ_{ij} . We show next that the nonzero components of the piezomagnetic response of MnF_2 correlate to the ferrotypes \mathcal{O}_{32^-} octupole.

Analyzing the different elements of $\tilde{\mathcal{S}}_{ijk}$, we see that the \mathcal{O}_{32^-} octupole, which has a ferrotypes ordering in MnF_2 , appears only when $i = x$, $j = y$, and $k = z$ and for the permutation of the indices. $\tilde{\mathcal{S}}_{ijk}$ being symmetric, all these elements are equal in magnitude. Similarly, analyzing the elements of other IR components, we find that the only other magnetic octupole component that has a ferrotypes ordering in MnF_2 is $\mathcal{Q}_{x^2-y^2}^{(\tau)}$, identified as the $x^2 - y^2$ quadrupole component of the toroidal moment density $\tau(\vec{r}) = \vec{r} \times \vec{\mu}(\vec{r})$. This leads to nonzero elements in the residue tensor $\tilde{\mathcal{R}}_{ijk}^{(5)}$, with $\tilde{\mathcal{R}}_{xyz}^{(5)} = \tilde{\mathcal{R}}_{yzx}^{(5)} \neq \tilde{\mathcal{R}}_{zxy}^{(5)}$. Combining the ferrotypes magnetic octupole components in MnF_2 and the tensor decomposition of the magnetic octupole \mathcal{O}_{ijk} , we obtain $\mathcal{O}_{xyz} = \mathcal{O}_{yxz} \neq \mathcal{O}_{zxy}$. This nicely correlates with the symmetry-allowed as well as experimentally observed components of piezomagnetic response for MnF_2 in Eq. (7), confirming the one-to-one correlation between the piezomagnetic response and the magnetic octupole tensor.

Finally, we also predict an *antipiezomagnetic* response in MnF_2 due to the antiferrotypes \mathcal{O}_{30} octupole. Upon application of stress, we expect an additional change in the Mn spin moments which is, however, opposite for the two Mn atoms so that their contributions cancel each other, leading to a zero net magnetization. Here, the tensor decomposition guides us in predicting which spin components will change due to an applied strain with a certain orientation. Therefore, we follow the same procedure as before and analyze first the elements of the symmetric traceless $\tilde{\mathcal{S}}_{ijk}$ to identify the elements of $\tilde{\mathcal{S}}_{ijk}$ in which the \mathcal{O}_{30} octupole appears. These are $\tilde{\mathcal{S}}_{xxz} = \tilde{\mathcal{S}}_{yyz} \neq \tilde{\mathcal{S}}_{zzz}$. The elements with symmetric permutation of these indices are also allowed. For these same elements of the residue tensors $\tilde{\mathcal{R}}_{ijk}^{(5)}$ and $\tilde{\mathcal{R}}_{ijk}^{(3)}$, we find that only $\tilde{\mathcal{R}}_{xxz}^{(3)} = \tilde{\mathcal{R}}_{yyz}^{(3)} \neq \tilde{\mathcal{R}}_{zzx}^{(3)} = \tilde{\mathcal{R}}_{zyy}^{(3)}$ are nonzero due to the existence of the antiferrotypes multipole $t_z^{(\tau)}$, defined as the z component of the moment of the toroidal moment density, in MnF_2 . This means that if both \mathcal{O}_{30} and $t_z^{(\tau)}$ were ferrotypes, we would have the following nonzero components in the piezomagnetic response:

$$\Lambda_{xxz} = \Lambda_{yyz}, \quad \Lambda_{zxx} = \Lambda_{zyy}, \quad \text{and} \quad \Lambda_{zzz}. \quad (8)$$

However, since, in fact, \mathcal{O}_{30} and $t_z^{(\tau)}$ have antiferrotypes arrangement in MnF_2 , the first equality in the above equation instead indicates that a spin component along \hat{x} (\hat{y}) will develop at individual Mn sites if we apply a shearing stress σ_{xz} (σ_{yz}) to the structure, with the developed

spin components having an antiparallel alignment between the Mn sites, so that there is no net magnetization along \hat{x} (\hat{y}). We refer to this effect as an antipiezomagnetic effect due to the generation of antiparallel spin components upon application of stress, in analogy to the piezomagnetic effect, where parallel spin moments are generated to give rise to a net change in magnetization.

2. DFT results for MnF_2

Next, to computationally verify our symmetry-guided prediction of an antipiezomagnetic effect and to better understand the microscopic details of both piezo- and antipiezomagnetic effects, we explicitly study the effect of a shear stress σ_{xz} (σ_{yz}) on the magnetism of MnF_2 within the DFT framework. The results of our calculations are depicted in Fig. 5. As is clear from Figs. 5(a) and 5(c), application of shear stress σ_{xz} (σ_{yz}) generates a net moment along \hat{y} (\hat{x}), as expected due to the piezomagnetic effect. In addition, as shown in Figs. 5(b) and 5(d), a tiny spin

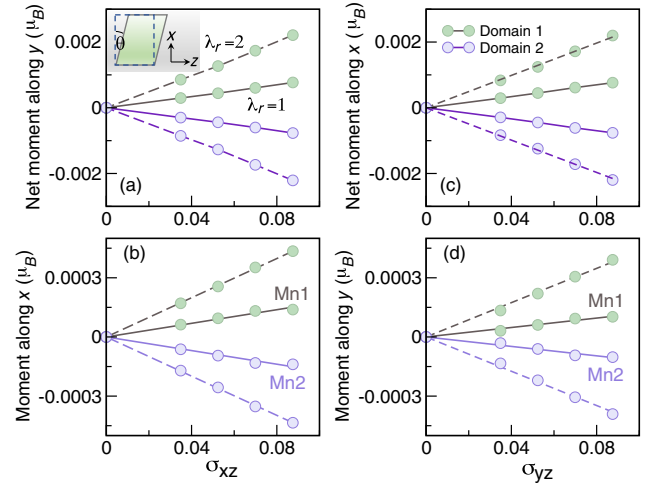


FIG. 5. Piezo- and antipiezomagnetic effects in MnF_2 . The variation of (a) the net magnetic moment along the y direction and (b) the individual Mn magnetic moments along the x direction as the shear strain σ_{xz} is varied. The inset in (a) depicts the schematic of the deformed shape of the unit cell under shear strain σ_{xz} (solid line) with respect to the undeformed tetragonal unit cell (dashed line). The shear strain $\sigma_{xz} = \tan \theta$ is determined by the deviation angle θ . The variations of (c) the net magnetic moment along x direction and (d) the individual Mn magnetic moments along the y direction as a function of the shear strain σ_{yz} , depicting the piezomagnetic and antipiezomagnetic effects driven by ferrotypes and antiferrotypes magnetic octupoles in MnF_2 . For the piezomagnetic effects in (a) and (c), the variations are shown for two different magnetic domains (in green and blue data points), while for antipiezomagnetic effects the variations of local spin magnetic moments (in green and blue data points) at two Mn atoms are shown. In both cases, variations are also shown for two different strengths of the spin-orbit coupling constant, viz., $\lambda_r = 1$ (solid line) and $\lambda_r = 2$ (dashed line). The parameter λ_r is defined in the caption of Fig. 2.

component appears along \hat{x} (\hat{y}) at the individual Mn sites with an antiparallel orientation at the neighboring Mn site, corresponding to the predicted antipiezomagnetic effect.

We see from Fig. 5 that both piezo- and antipiezomagnetic responses are linear in nature. Also, in both cases, the generated moments reverse their directions in the opposite antiferromagnetic domain. Such a reversal of moment direction is consistent with experimental reports and can be understood from the fact that both \mathcal{O}_{32^-} and \mathcal{O}_{30} octupoles have opposite signs in the opposite antiferromagnetic domains. We note that the generated moment due to the piezomagnetic response is larger than that due to the antipiezomagnetic response. This can be understood from the fact that the former corresponds to the $[\mathcal{O}_{32^-} - (\mathcal{Q}_{x^2-y^2}^{(\tau)}/6)]$ term of the magnetic octupole tensor, while the latter corresponds to $[-(\mathcal{O}_{30}/10) + (t_z^{(\tau)}/3)]$, and confirms that the piezo- and antipiezomagnetic responses depend on the magnitudes of the magnetic octupoles.

Furthermore, to understand the importance of spin-orbit interaction on these effects, we artificially double the strength of the spin-orbit coupling in our calculation, and, as depicted in Fig. 5, this results in an enhancement in the generated moment for both cases. This suggests that, unlike the magnetic Compton scattering described in the next section, both piezo- and antipiezomagnetic effects are relativistic effects. Physically, this can be understood from the fact that the stress applied to the structure needs to be coupled to the magnetization density of the system, which is mediated via spin-orbit interaction. We note that the dependence on the spin-orbit coupling strength also helps to predict the hierarchy of the piezo- and antipiezomagnetic effects in different materials. For example, the relativistic piezo- and antipiezomagnetic effects are expected to be much stronger in CoF_2 compared to MnF_2 due to the strong spin-orbit interaction of the Co atoms in the former.

The predicted antipiezomagnetic effect should be experimentally observable by detecting the resulting spin canting in the presence of an applied stress. While the early experiments [80], indeed, indicated rotation of spins upon application of a shear stress so that an antiparallel spin component is generated in addition to a net magnetization in a piezomagnetic effect, confirmation of the antipiezomagnetic effect would require further measurements to verify the linear generation and the switching of canted moments. Another possibility of experimental verification would be to apply a dynamical stress, causing opposite stresses on the two Mn sublattices, so that the antipiezomagnetic effect would lead to a net magnetization. Our work, correlating the piezo- and antipiezomagnetic effects to the magnetic octupoles, serves as a guideline for future observation and manipulation of spin arrangements using strain [76,77].

C. Direct detection of magnetic octupoles: Magnetic Compton profile in an antiferromagnet

The Compton scattering [82] of x-ray photons, which was an early confirmation of quantum mechanical behavior, is a widely used technique today in fields as diverse as radiobiology, astrophysics, and condensed matter physics. In condensed matter systems, it is used to measure the electron density in momentum space or in an extension known as magnetic Compton scattering, the spin-dependent electron momentum density [83]:

$$J_{\text{mag}}(p_z) = \int \int [\rho_{\uparrow}(\vec{p}) - \rho_{\downarrow}(\vec{p})] dp_x dp_y. \quad (9)$$

Here, J_{mag} is the magnetic Compton profile (MCP), the key quantity measured in the magnetic Compton scattering measurements. As defined above, it is the one-dimensional projection of the spin-polarized electron momentum density $[\rho_{\uparrow}(\vec{p}) - \rho_{\downarrow}(\vec{p})]$ along the x-ray scattering vector p_z . Here, $\rho_{\uparrow}(\vec{p})$ and $\rho_{\downarrow}(\vec{p})$ are, respectively, the up and down spin-polarized electron density in momentum space. The integrals over p_x and p_y [Eq. (9)] are performed over the plane in momentum space that is perpendicular to the direction of x-ray scattering vector along p_z .

Magnetic Compton scattering has been extensively applied to ferri- and ferromagnetic systems (with nonzero magnetization) [84–96] to extract spin polarizations at Fermi surfaces [93–95]. In one of our recent works, we proposed that a spin-polarized electron density can also exist in the momentum space of nonmagnetic systems, provided that the inversion symmetry is broken, leading to a MCP [72]. To date, however, MCP has not been proposed or measured in conventional antiferromagnets, because the up and down spin-polarized bands are degenerate, leading to vanishing spin-polarized electron density in momentum space. Here, we show that the spin splitting of the energy bands in antiferromagnets with ferrottype magnetic octupoles results in a nonzero MCP, despite the zero net magnetization. This, in turn, facilitates the MCP as a direct probe for existence of ferrottype magnetic octupoles.

To verify the nonzero MCP for our example material MnF_2 , we explicitly compute the MCP using the methods implemented in the ELK code (see the computational details in Appendix A). The computed MCP of MnF_2 along the [110] direction in momentum space is shown in Fig. 6(a). Here, the scattering vector p_z is along the [110] direction, and the integral in the Compton profile is performed over the (110) plane (perpendicular to the scattering vector [110]). This is, to our knowledge, the first identification of a MCP in an AFM. We note that the MCP is present even without including spin-orbit effects, as expected due to the nonrelativistic spin splitting in MnF_2 . Note also that the integral of the MCP is zero, consistent with the net vanishing moment in the system.

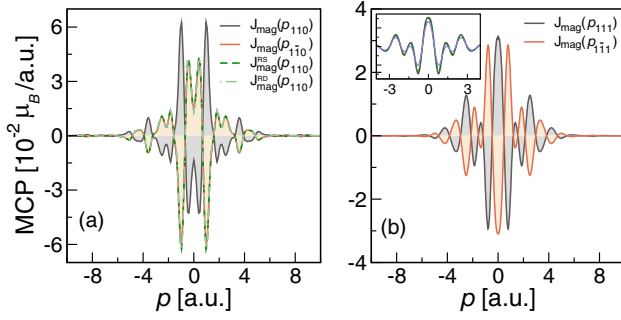


FIG. 6. MCPs of MnF_2 along (a) $[110]$ and $[1\bar{1}0]$ and (b) $[111]$ and $[1\bar{1}\bar{1}]$ directions in the momentum space. The reversal of the profiles is apparent from (a) and (b) as the momentum direction changes by C_4 rotation. (a) also depicts the MCPs along the $[110]$ direction, $J_{\text{mag}}^{\text{RS}}(p_{110})$ and $J_{\text{mag}}^{\text{RD}}(p_{110})$, for the hypothetical modified structure and for the reversed magnetic domain, respectively. In both cases, the MCP switches sign compared to the profile of MnF_2 along the same momentum direction. The inset shows the comparison of the computed profile (black line) with the convoluted profiles for the experimental resolutions of 0.22 (green line) and 0.44 a.u. (violet line).

The characteristics of the computed MCP are quite different from those of nonmagnetic ferroelectrics. First, the computed MCP is symmetric in \vec{p} in contrast to the antisymmetric MCP in ferroelectrics [72]. This follows from the symmetric and antisymmetric spin splitting in MnF_2 and ferroelectrics, respectively. More importantly, however, the magnitude of the MCP in MnF_2 is larger by about an order of magnitude compared to the computed values for the ferroelectrics PbTiO_3 and GeTe [72]. This again is associated with the large NRSS of the bands in contrast to the weak relativistic spin splitting of the bands in ferroelectrics. Finally, as shown in Fig. 6(a), the MCP in MnF_2 changes sign as the momentum direction is changed from the $[110]$ to the $[1\bar{1}0]$ direction, unlike the case of ferroelectrics for which the profile, being antisymmetric, switches sign as $\vec{p} \rightarrow -\vec{p}$. Such sign reversal of the MCP in MnF_2 is understandable from the reversal of the spin splitting as the momentum direction changes from $[110]$ to $[1\bar{1}0]$ [see Fig. 4(b)].

Since the magnetic octupole leads to the spin splitting of the bands, which, in turn, gives rise to the MCP, the MCP provides a direct measurement of the existence of ferroically ordered magnetic octupoles in MnF_2 . For further confirmation, we compute the MCPs for the cases of the reversed structure and the other AFM domain (described in Sec. III B), for both of which the ferrotype \mathcal{O}_{32^-} magnetic octupole reverses sign. Indeed, the computed MCPs, shown in Fig. 6(a), reverse the sign of their profile, in agreement with our expectation.

1. Proposed experimental setup

The measurement setup needed to detect magnetic octupoles using MCP will be similar to that of a conventional

magnetic Compton scattering experiment with circularly polarized light. Generally, the measurements are performed in backscattering geometry with either parallel spin and momentum directions or along a momentum direction that has at least one component along the direction of the spin polarization. Since the spin polarization direction in MnF_2 is along \hat{z} , we further compute the MCPs along the $[111]$ direction in reciprocal space. As depicted in Fig. 6(b), the computed MCP, although smaller compared to that along $[110]$, still has a much larger magnitude compared to the case of a ferroelectric. Furthermore, the convoluted magnetic Compton profiles for two different resolutions of 0.22 and 0.44 a.u., as shown in the inset in Fig. 6(b), suggest that the computed magnetic Compton profile should be discernible in experiments even with a moderate resolution of 0.44 a.u.

Note that the integral of the magnetic Compton profile, $\int_{-\infty}^{\infty} J_{\text{mag}}(p_z) dp_z$, gives the net spin magnetic moment in the unit cell. For the computed magnetic Compton profile, shown in Fig. 6, the integral becomes zero as expected due to the absence of any net magnetization. This, along with the reversal of the magnetic Compton profile with the C_4 rotation of the momentum direction, as discussed above, would be a signature of the unusual magnetism related to the magnetic octupoles and nonrelativistic spin splitting in magnetic Compton scattering.

We note that, since the two antiferromagnetic domains lead to opposite spin splitting, it is crucial to carry out the measurements on a single antiferromagnetic domain of MnF_2 . Such a single antiferromagnetic domain can be obtained by the simultaneous application of a uniaxial stress and a magnetic field while cooling the sample through the Néel temperature $T_N \approx 67$ K [47,81]. Interestingly, as stated before, the combination of stress and magnetic field is, in fact, the conjugate field of a magnetic octupole, and, as described before, each of the antiferromagnetic domains can indeed be identified as a ferro-octupolar domain. Such a single magnetic domain is also referred to as a piezomagnetic domain due to its close connection to the piezomagnetic effect in MnF_2 [81], driven by the ferroic magnetic octupoles as discussed in the previous section.

V. DISCUSSION AND OUTLOOK

In summary, using MnF_2 as an example material, we have shown that the order parameter of centrosymmetric magnets with NRSS and zero net magnetization is the magnetic octupole, since it is the lowest-order ferroically ordered magnetic quantity in this case. The magnetic octupolar description has the advantage that it not only provides a convenient description of the NRSS, but also provides the platform for the systematic control (both magnitude and sign) of the NRSS, which is highly desirable for the rational design of such materials. Furthermore, complementary to the spin-group theory [28], the k -space representation of the magnetic octupole dictates the direction in the momentum space along which the NRSS occurs,

which drastically reduces the computational effort to search for NRSS throughout the entire BZ. More importantly, identifying the magnetic domains as the ferro-octupolar domain reveals the conjugate field—a combined stress and magnetic field—required for selection of one of the magnetic domains. We note that, since the NRSS is opposite for the two magnetic domains, selection of a particular magnetic domain is essential for any practical usage.

In addition to the above-mentioned key insight into the NRSS, we also demonstrate the linear piezomagnetic effect as a universal effect associated with magnetic octupoles, independent of the occurrence of NRSS. They also allow us to predict an as-yet-unobserved nonlinear magnetoelectric effect, in which a quadratic (or bilinear) electric field (\vec{E}) induces a linear magnetization (\vec{M}), of the form $M_i = \alpha_{ijk} E_j E_k$, driven by the ferroic arrangement of the magnetic octupole [65] as well as an antipiezomagnetic effect resulting from an additional antiferroic arrangement of different magnetic octupoles. Finally, we propose magnetic Compton scattering for the direct detection of magnetic octupoles in such unconventional antiferromagnets with NRSS.

We note that, with the change of spin-quantization axis, different magnetic octupole components appear, corresponding to the different spin polarization axes of the spin-split bands. Consequently, the k -space representation of the corresponding magnetic octupole components represents the NRSS along the same momentum direction but with different spin polarization directions. Thus, for the same crystal structure and pattern of magnetic ordering, a different spin axis may result in an (anti)piezomagnetic response with different nonzero components, or the magnetic Compton profile may appear for a different spin quantization axis but along the same directions in momentum space, etc. However, the analysis and recipe to investigate these remain the same. Conversely, systems with the same structural and magnetic symmetries would allow for the same components of the magnetic octupoles. For example, isostructural CoF_2 has the same nonzero magnetic octupole components as MnF_2 .

It is important to point out here that, although we specifically discussed the case of MnF_2 , the presence of magnetic octupoles is general to all NRSS AFMs with d -wave splitting. This also includes materials that exhibit bulk d -wave spin splitting, e.g., CuF_2 [28]. For the monoclinic structure [97] (unique axis c) of CuF_2 and collinear spins along \hat{z} [28], the k -space representations of the existing magnetic octupole components \mathcal{O}_{31} ($Q_{yz}^{(\tau)}, I_x^{(\tau)}$) and \mathcal{O}_{31^-} ($Q_{xz}^{(\tau)}, I_y^{(\tau)}$) are, respectively, $k_x k_z m_z$ and $k_y k_z m_z$, thus leading to bulklike d -wave spin splitting that also depends on k_z . In general, the magnetic octupoles have the inherent d -wave symmetry and are the lowest-order symmetry-allowed ferrottype magnetic multipole, as discussed in Sec. III. As a result, they always provide a convenient description of the d -wave NRSS. Consequently, the MCP and the piezomagnetic effect are also universal to AFMs

with d -wave NRSS. We note, however, that the piezomagnetic effect is a relativistic effect, and, hence, it can also occur in systems where the magnetic octupoles are induced by the spin-orbit interaction or noncollinearity of the spins, beyond the collinear AFMs with d -wave NRSS.

We note that centrosymmetric antiferromagnets with NRSS may also have higher-order ferroically ordered even-parity magnetic multipoles in addition to their ferromagneto-octupolar order. These higher-order multipoles, if they exist even without spin-orbit interaction, are relevant for describing NRSS with g -wave or i -wave symmetry. For example, Fe_2O_3 in its low-temperature state with magnetic moments oriented along the symmetry axis, which is reported to have a g -wave spin splitting [31], allows for a magnetic triacontadipole in addition to the magnetic octupole. Interestingly, while the ferrottype magnetic octupole components, in this case, are induced by the spin-orbit interaction, the magnetic triacontadipole has nonzero components with ferrottype ordering even without the spin-orbit coupling. The g -wave symmetry of the spatial part of the magnetic triacontadipole suggests a connection between this rank-5 even-parity magnetic multipole and the corresponding g -wave NRSS, which is an interesting direction for future study. It is important to point out here that the spin-orbit-induced, ferrottype magnetic octupole components \mathcal{O}_{33} and $Q_{z^2}^{(\tau)}$ in Fe_2O_3 allow for a piezomagnetic effect and the symmetry-allowed response components can be conveniently described by these magnetic octupole components, following the same procedure as described in Sec. IV B.

In addition to providing important insight into the newly discovered unconventional antiferromagnets with NRSS, the results presented here are relevant for the prolonged effort to reveal and detect the magnetic octupolar phase [65,98–108], as well as for potential applications through strain engineering of antiferromagnetism via the piezo- or antipiezomagnetic effect in spintronic devices. We note that magnetic octupoles are also likely to be relevant for the reported spin-phonon interaction [109,110] and surface magnetization [111] in MnF_2 and could shed light on the reported strong magnetic anisotropy in doped FeSb_2 [49].

Merging the seemingly disconnected fields of hidden order, antiferromagnetic spintronics, and inelastic scattering techniques, our work opens up new directions for exploration which we hope will motivate both theoretical and experimental investigation in the near future.

ACKNOWLEDGMENTS

We thank Steve Collins, Jon Duffy, Maximilian E. Merkel, Urs Staub, Andrea Urru, and Sophie Weber for stimulating discussions. We also thank Tomáš Jungwirth, Mathias Kläui, Jairo Sinova, Libor Šmejkal, and Alex Zunger for their useful feedback on the manuscript.

N. A. S. and S. B. were supported by the ERC under the EU's Horizon 2020 Research and Innovation Programme Grant No. 810451 and by the ETH Zurich. Computational resources were provided by ETH Zurich's Euler cluster and the Swiss National Supercomputing Centre, Project ID No. eth3.

APPENDIX A: COMPUTATIONAL DETAILS

The electronic structure of MnF_2 has been computed using the linearized augmented plane wave method as implemented in the ELK code [112]. We use the LDA + SOC + U formalism, with $U_{\text{eff}} = 5$ eV at the Mn site [26]. A basis set of $l_{\text{max}(apw)} = 8$, a $5 \times 5 \times 7$ k -point sampling of the Brillouin zone are used to achieve self-consistency. The product of the muffin-tin radius (2.4 and 2 a.u. for Mn and F, respectively) and the maximum reciprocal lattice vector is taken to be 7. The magnetic Compton profile and the atomic-site multipoles are computed using the extended versions [9,113] of the ELK code. The spin-polarized electron momentum densities are calculated and projected

onto the selected momentum directions (\vec{p}) to obtain the magnetic Compton profile following the implementations, reported in Ref. [113]. The computed MCP is scaled to the factor that normalizes the valence contribution of the total Compton profile to the total number of valence electrons per formula unit of MnF_2 in the calculation, which is 29 in this case. For the computation of atomic-site multipoles, the density matrix $\rho_{l_1 m_1, l_2 m_2}$ is decomposed into the tensor moments, of which the parity-even tensor moments have contributions from terms with $l_1 = l_2$. We, therefore, evaluate both $d-d$ and $p-p$ matrix element contributions for the multipoles at the Mn site. The octupole components \mathcal{O}_{lm} , $\mathcal{Q}_{ij}^{(\tau)}$, and $t_i^{(\tau)}$ correspond to the irreducible spherical tensor w^{kpr} , where the spatial index $k = 2$, spin index $p = 1$, and $r = 3, 2$, and 1, respectively. The allowed value of the spherical component t of w^{kpr} is determined by r , such that $-r \leq t \leq r$, leading to seven, five, and three components of \mathcal{O}_{lm} , $\mathcal{Q}_{ij}^{(\tau)}$, and $t_i^{(\tau)}$, respectively. The $l_1 l_2$ matrix element of w_t^{kpr} reads as [57,114]

$$\begin{aligned} \langle w_t^{kpr} \rangle_{l_1 l_2} &= \sum_{m_1, m_2} \sum_{\sigma_1, \sigma_2} \langle l_1, m_1, \frac{1}{2}, \sigma_1 | w_t^{kpr} | l_2, m_2, \frac{1}{2}, \sigma_2 \rangle \\ &= \frac{1}{n_{kpr}} \sum_{m_1, m_2} \sum_{\sigma_1, \sigma_2} \sum_{x, y} (-1)^{k-x} (-1)^{p-y} (-1)^{l_1 - m_1} (-1)^{\frac{1}{2} - \sigma_1} \\ &\quad \times \frac{1}{n_{l_1 l_2 k}} \frac{1}{n_{\frac{1}{2} p}} \begin{pmatrix} k & r & p \\ -x & t & -y \end{pmatrix} \begin{pmatrix} l_1 & k & l_2 \\ -m_1 & x & m_2 \end{pmatrix} \begin{pmatrix} \frac{1}{2} & p & \frac{1}{2} \\ -\sigma_1 & y & \sigma_2 \end{pmatrix} \rho_{l_1 m_1, l_2 m_2}^{\nu \sigma_1 \sigma_2}. \end{aligned} \quad (\text{A1})$$

Here, the quantities in round brackets are Wigner-3j coefficients, n_{kpr} is a normalization factor, $n_{l_1 l_2 k} = [(l_1 + l_2)! / \sqrt{(l_1 + l_2 - k)! (l_1 + l_2 + k + 1)!}]$, and $n_{\frac{1}{2} p} = (1 / \sqrt{(p + 2)!})$ [57,114]. ρ^ν contains the time-reversal even ($\nu = 0$) and odd ($\nu = 1$) parts of the density matrix.

The electronic structure of MnF_2 is also computed within the plane-wave-based projector augmented wave [115,116] method as implemented in the Vienna *ab initio* simulation package (VASP) [117,118], and the results agree well with that computed using the ELK code. The atomic relaxations in presence of shear strain in the piezomagnetic effect are carried out until the Hellman-Feynman force on each atom becomes less than 0.01 eV/Å. The constrained multipole calculations are performed using the methodology developed in Ref. [119]. The modifications to the VASP code are openly accessible and documented on GitHub [120]. Within this approach, a shift matrix, corresponding to the desired constrained multipole, is added to the potential, keeping the crystal structure and magnetic configuration unaltered. The values of both charge and magnetic multipoles are then computed once self-consistency is achieved.

APPENDIX B: IRREDUCIBLE COMPONENTS OF THE MAGNETIC OCTUPOLE

Here, we write down the explicit forms of the different IR components of the magnetic octupole \mathcal{O}_{ijk} , as described in Sec. IV B, following Ref. [65]. The totally symmetric traceless part $\tilde{\mathcal{S}}_{ijk}$ is given by

$$\tilde{\mathcal{S}}_{1jk} = \frac{1}{20} \begin{bmatrix} 5\mathcal{O}_{33} - 3\mathcal{O}_{31} & 5\mathcal{O}_{33} - \mathcal{O}_{31^-} & 2(5\mathcal{O}_{32} - \mathcal{O}_{30}) \\ 5\mathcal{O}_{33^-} - \mathcal{O}_{31^-} & -(5\mathcal{O}_{33} + \mathcal{O}_{31}) & 20\mathcal{O}_{32^-} \\ 2(5\mathcal{O}_{32} - \mathcal{O}_{30}) & 20\mathcal{O}_{32^-} & 4\mathcal{O}_{31} \end{bmatrix}. \quad (\text{B1})$$

Note that, $\tilde{\mathcal{S}}_{ijk}$ being completely symmetric, the rest of the components can be obtained from $\tilde{\mathcal{S}}_{1jk}$ by permutation of the indices and $\tilde{\mathcal{S}}_{222} = -(5\mathcal{O}_{33^-} + \mathcal{O}_{31^-})$ and $\tilde{\mathcal{S}}_{333} = 4\mathcal{O}_{30}$. Note that the elements of $\tilde{\mathcal{S}}_{ijk}$, i.e., \mathcal{O}_{lm} in Eq. (B1), can be built from the spherical harmonics of $l = 3$ with components $m = -3, -2, \dots, 2, 3$.

The components of the five-dimensional residual tensor $\tilde{\mathcal{R}}_{ijk}^{(5)}$ can be expressed in terms of the five components of the quadrupole moment $Q_{ij}^{(\tau)}$ of the toroidal moment density $\vec{\tau}(\vec{r}) = \vec{r} \times \vec{\mu}(\vec{r})$, viz.,

$$\begin{aligned} \tilde{\mathcal{R}}_{1jk}^{(5)} &= \frac{1}{3} \begin{bmatrix} 0 & -Q_{xz}^{(\tau)} & Q_{xy}^{(\tau)} \\ -Q_{xz}^{(\tau)} & -2Q_{yz}^{(\tau)} & -\frac{1}{2}(Q_{x^2-y^2}^{(\tau)} + 3Q_{z^2}^{(\tau)}) \\ Q_{xy}^{(\tau)} & -\frac{1}{2}(Q_{x^2-y^2}^{(\tau)} + 3Q_{z^2}^{(\tau)}) & 2Q_{yz}^{(\tau)} \end{bmatrix}, \\ \tilde{\mathcal{R}}_{2jk}^{(5)} &= \frac{1}{3} \begin{bmatrix} 2Q_{xz}^{(\tau)} & Q_{yz}^{(\tau)} & -\frac{1}{2}(Q_{x^2-y^2}^{(\tau)} - 3Q_{z^2}^{(\tau)}) \\ Q_{yz}^{(\tau)} & 0 & -Q_{xy}^{(\tau)} \\ -\frac{1}{2}(Q_{x^2-y^2}^{(\tau)} - 3Q_{z^2}^{(\tau)}) & -Q_{xy}^{(\tau)} & -2Q_{xz}^{(\tau)} \end{bmatrix}, \\ \tilde{\mathcal{R}}_{3jk}^{(5)} &= \frac{1}{3} \begin{bmatrix} -2Q_{xy}^{(\tau)} & Q_{x^2-y^2}^{(\tau)} & -2Q_{yz}^{(\tau)} \\ Q_{x^2-y^2}^{(\tau)} & 2Q_{xy}^{(\tau)} & Q_{xz}^{(\tau)} \\ -2Q_{yz}^{(\tau)} & Q_{xz}^{(\tau)} & 0 \end{bmatrix}. \end{aligned} \quad (\text{B2})$$

Finally, the components of the three-dimensional residual tensor $\tilde{\mathcal{R}}_{ijk}^{(3)}$ can be expressed in terms of the three components of the moment $\vec{t}^{(\tau)}$ of the toroidal moment density $\vec{\tau}(\vec{r})$:

$$\begin{aligned} \tilde{\mathcal{R}}_{1jk}^{(3)} &= \frac{1}{3} \begin{bmatrix} 0 & t_y^{(\tau)} & t_z^{(\tau)} \\ t_y^{(\tau)} & -2t_x^{(\tau)} & 0 \\ t_z^{(\tau)} & 0 & -2t_x^{(\tau)} \end{bmatrix}, \\ \tilde{\mathcal{R}}_{2jk}^{(3)} &= \frac{1}{3} \begin{bmatrix} -2t_y^{(\tau)} & t_x^{(\tau)} & 0 \\ t_x^{(\tau)} & 0 & t_z^{(\tau)} \\ 0 & t_z^{(\tau)} & -2t_y^{(\tau)} \end{bmatrix}, \\ \tilde{\mathcal{R}}_{3jk}^{(3)} &= \frac{1}{3} \begin{bmatrix} -2t_z^{(\tau)} & 0 & t_x^{(\tau)} \\ 0 & -2t_z^{(\tau)} & t_y^{(\tau)} \\ t_x^{(\tau)} & t_y^{(\tau)} & 0 \end{bmatrix}. \end{aligned} \quad (\text{B3})$$

TABLE I. Character table for the D_{4h} point group.

D_{4h}	E	$2C_4(z)$	C_2	$2C_2'$	$2C_2''$	i	$2S_4$	σ_h	$2\sigma_v$	$2\sigma_d$
A_{1g}	+1	+1	+1	+1	+1	+1	+1	+1	+1	+1
A_{2g}	+1	+1	+1	-1	-1	+1	+1	+1	-1	-1
B_{1g}	+1	-1	+1	+1	-1	+1	-1	+1	+1	-1
B_{2g}	+1	-1	+1	-1	+1	+1	-1	+1	-1	+1
E_g	+2	0	-2	0	0	+2	0	-2	0	0
A_{1u}	+1	+1	+1	+1	+1	-1	-1	-1	-1	-1
A_{2u}	+1	+1	+1	-1	-1	-1	-1	-1	+1	+1
B_{1u}	+1	-1	+1	+1	-1	-1	+1	-1	-1	+1
B_{2u}	+1	-1	+1	-1	+1	-1	+1	-1	+1	-1
E_u	+2	0	-2	0	0	-2	0	+2	0	0

APPENDIX C: CHARACTER TABLE FOR THE D_{4h} POINT GROUP

The character table for the D_{4h} point group symmetry of the crystal structure of MnF_2 is listed in Table I.

APPENDIX D: DFT BAND STRUCTURES IN ABSENCE OF MAGNETISM

The computed band structure in the absence of magnetism is shown in Fig. 7, depicting the splitting between bands of two different sublattice contributions along

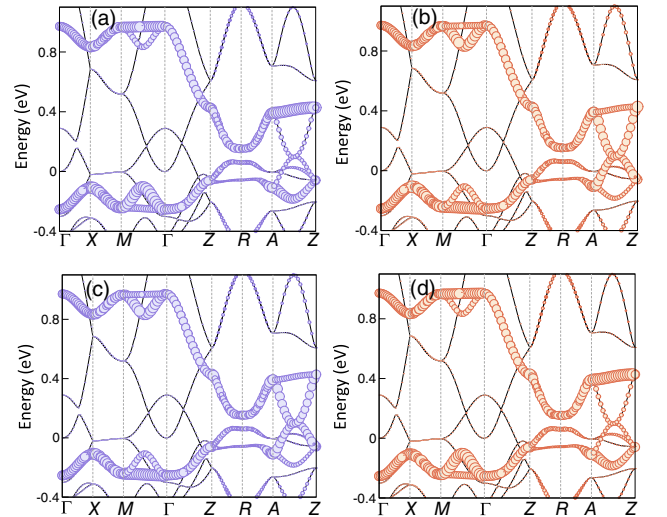


FIG. 7. Nonmagnetic band structure of MnF_2 , showing the d_{xz} and d_{yz} orbital contributions for the (a) Mn1 and (b) Mn2 sublattices. (c) and (d) depict the same for the hypothetical modified structure, indicating a reversal of Mn1 and Mn2 sublattice contributions for the modified structure.

$\Gamma \rightarrow M$. For example, for the pair of bands around 1 eV along $\Gamma \rightarrow M$, the top band has predominant contributions from the Mn1 sublattice, while the bottom band is predominantly of Mn2 sublattice character. For the modified structure, described in Sec. III B, the computed atom and orbital projected band structure shows that the band structure remains identical except that the sublattice characters of the same pair of bands are reversed.

APPENDIX E: TIGHT-BINDING PARAMETERS

The realistic tight-binding parameters of the Hamiltonian (2), i.e., the effective $d-d$ hoppings t_i ($i = 1, 4$) and the on-site energies ε_i ($i = 1, 2$) in Eq. (3), are extracted from the DFT calculations by downfolding the effect of the F- p orbitals using the NMTO method [75]. The computed parameters are listed in Table II.

TABLE II. Tight-binding parameters of the Hamiltonian (2), extracted using the NMTO method.

d-d hopping parameters (Ry)				On-site energies (Ry)	
t_1	t_2	t_3	t_4	ε_1	ε_2
0.0036	-0.0038	0.0040	0.0034	-0.1385	-0.0339

- [1] R. W. Millar, *The specific heats at low temperatures of manganous oxide, manganous-manganic oxide and manganese dioxide*, *J. Am. Chem. Soc.* **50**, 1875 (1928).
- [2] R. W. Tyler, *The magnetic susceptibility of MnO as a function of the temperature*, *Phys. Rev.* **44**, 776 (1933).
- [3] L. Néel, *Propriétés magnétiques de l'état métallique et énergie d'interaction entre atomes magnétiques*, *Ann. Phys. (Paris)* **11**, 232 (1936).
- [4] H. Bizette, C. F. Squire, and B. Tsai, *Le point de transition λ de la susceptibilité magnétique du protoxyde de manganèse MnO*, *C.R. Hebd. Seances Acad. Sci.* **207**, 449 (1938).
- [5] G. Shull and J. S. Smart, *Detection of antiferromagnetism by neutron diffraction*, *Phys. Rev.* **76**, 1256 (1949).
- [6] P. A. McClarty and J. G. Rau, *Landau theory of altermagnetism*, [arXiv:2308.04484](https://arxiv.org/abs/2308.04484).
- [7] C. Ederer and N. A. Spaldin, *Towards a microscopic theory of toroidal moments in bulk periodic crystals*, *Phys. Rev. B* **76**, 214404 (2007).
- [8] B. B. V. Aken, J. P. Rivera, H. Schmid, and M. Fiebig, *Observation of ferrotoroidic domains*, *Nature (London)* **449**, 702 (2007).
- [9] N. A. Spaldin, M. Fechner, E. Bousquet, A. Balatsky, and L. Nordström, *Monopole-based formalism for the diagonal magnetoelectric response*, *Phys. Rev. B* **88**, 094429 (2013).
- [10] N. A. Spaldin, M. Fiebig, and M. Mostovoy, *The toroidal moment in condensed-matter physics and its relation to the magnetoelectric effect*, *J. Phys. Condens. Matter* **20**, 434203 (2008).
- [11] C. Binek and B. Doudin, *Magnetolectronics with magnetoelectrics*, *J. Phys. Condens. Matter* **17**, L39 (2005).
- [12] P. Borisov, A. Hochstrat, X. Chen, W. Kleemann, and C. Binek, *Magnetolectric switching of exchange bias*, *Phys. Rev. Lett.* **94**, 117203 (2005).
- [13] H. Watanabe and Y. Yanase, *Group-theoretical classification of multipole order: Emergent responses and candidate materials*, *Phys. Rev. B* **98**, 245129 (2018).
- [14] S. Hayami, M. Yatsushiro, Y. Yanagi, and H. Kusunose, *Classification of atomic-scale multipoles under crystallographic point groups and application to linear response tensors*, *Phys. Rev. B* **98**, 165110 (2018).
- [15] F. Thöle, A. Keliri, and N. A. Spaldin, *Concepts from the linear magnetoelectric effect that might be useful for antiferromagnetic spintronics*, *J. Appl. Phys.* **127**, 213905 (2020).
- [16] B. Göbel, A. Mook, J. Henk, and I. Mertig, *Magnetolectric effect and orbital magnetization in skyrmion crystals: Detection and characterization of skyrmions*, *Phys. Rev. B* **99**, 060406(R) (2019).
- [17] S. Bhowal and N. A. Spaldin, *Magnetolectric classification of skyrmions*, *Phys. Rev. Lett.* **128**, 227204 (2022).
- [18] Y. Gao and D. Xiao, *Orbital magnetic quadrupole moment and nonlinear anomalous thermoelectric transport*, *Phys. Rev. B* **98**, 060402(R) (2018).
- [19] S. Pekar and G. Rashba, *Combined resonance in crystals in inhomogeneous magnetic fields*, *Zh. Eksp. Teor. Fiz.* **47**, 1927 (1964), http://www.jetp.ras.ru/cgi-bin/dn/e_020_05_1295.pdf.
- [20] E. Rashba, *Properties of semiconductors with an extremum loop. I. cyclotron and combinational resonance in a magnetic field perpendicular to the plane of the loop*, *Sov. Phys. Solid State* **2**, 1109 (1960).
- [21] Y. A. Bychkov and E. I. Rashba, *Oscillatory effects and the magnetic susceptibility of carriers in inversion layers*, *J. Phys. C* **17**, 6039 (1984).
- [22] L. Šmejkal, R. González-Hernández, T. Jungwirth, and J. Sinova, *Crystal time-reversal symmetry breaking and spontaneous Hall effect in collinear antiferromagnets*, *Sci. Adv.* **6**, eaaz8809 (2020).
- [23] M. Naka, S. Hayami, H. Kusunose, Y. Yanagi, Y. Motome, and H. Seo, *Spin current generation in organic antiferromagnets*, *Nat. Commun.* **10**, 4305 (2019).
- [24] K.-H. Ahn, A. Hariki, K.-W. Lee, and J. Kuneš, *Antiferromagnetism in RuO₂ as d-wave Pomeranchuk instability*, *Phys. Rev. B* **99**, 184432 (2019).
- [25] S. Hayami, Y. Yanagi, and H. Kusunose, *Momentum-dependent spin splitting by collinear antiferromagnetic ordering*, *J. Phys. Soc. Jpn.* **88**, 123702 (2019).
- [26] L.-D. Yuan, Z. Wang, J.-W. Luo, E. I. Rashba, and A. Zunger, *Giant momentum-dependent spin splitting in centrosymmetric low-z antiferromagnets*, *Phys. Rev. B* **102**, 014422 (2020).
- [27] L.-D. Yuan, Z. Wang, J.-W. Luo, and A. Zunger, *Prediction of low-z collinear and noncollinear antiferromagnetic compounds having momentum-dependent spin*

- splitting even without spin-orbit coupling, *Phys. Rev. Mater.* **5**, 014409 (2021).
- [28] L. Šmejkal, J. Sinova, and T. Jungwirth, *Beyond conventional ferromagnetism and antiferromagnetism: A phase with nonrelativistic spin and crystal rotation symmetry*, *Phys. Rev. X* **12**, 031042 (2022).
- [29] L.-D. Yuan and A. Zunger, *Degeneracy removal of spin bands in antiferromagnets with non-interconvertible spin motif pair*, arXiv:2211.07803.
- [30] L.-D. Yuan, X. Zhang, C. Mera, and A. Zunger, *Uncovering hidden spin polarization of energy bands in antiferromagnets*, arXiv:2211.09921.
- [31] L. Šmejkal, J. Sinova, and T. Jungwirth, *Emerging research landscape of altermagnetism*, *Phys. Rev. X* **12**, 040501 (2022).
- [32] R. González-Hernández, L. Šmejkal, K. Výborný, Y. Yahagi, J. Sinova, T. Jungwirth, and J. Železný, *Efficient electrical spin splitter based on nonrelativistic collinear antiferromagnetism*, *Phys. Rev. Lett.* **126**, 127701 (2021).
- [33] D.-F. Shao, S.-H. Zhang, M. Li, C.-B. Eom, and E. Y. Tsymbal, *Spin-neutral currents for spintronics*, *Nat. Commun.* **12**, 7061 (2021).
- [34] A. Bose, N. J. Schreiber, R. Jain, D.-F. Shao, H. P. Nair, J. Sun, X. S. Zhang, D. A. Muller, E. Y. Tsymbal, D. G. Schlom, and D. C. Ralph, *Tilted spin current generated by the collinear antiferromagnet ruthenium dioxide*, *National electronics review* **5**, 267 (2022).
- [35] H. Bai, L. Han, X. Y. Feng, Y. J. Zhou, R. X. Su, Q. Wang, L. Y. Liao, W. X. Zhu, X. Z. Chen, F. Pan, X. L. Fan, and C. Song, *Observation of spin splitting torque in a collinear antiferromagnet RuO₂*, *Phys. Rev. Lett.* **128**, 197202 (2022).
- [36] S. Karube, T. Tanaka, D. Sugawara, N. Kadoguchi, M. Kohda, and J. Nitta, *Observation of spin-splitter torque in collinear antiferromagnetic RuO₂*, *Phys. Rev. Lett.* **129**, 137201 (2022).
- [37] L. Šmejkal, A. B. Hellenes, R. González-Hernández, J. Sinova, and T. Jungwirth, *Giant and tunneling magnetoresistance in unconventional collinear antiferromagnets with nonrelativistic spin-momentum coupling*, *Phys. Rev. X* **12**, 011028 (2022).
- [38] H. Reichlová, R. L. Seeger, R. González-Hernández, I. Kounta, R. Schlitz, D. Kriegner, P. Ritzinger, M. Lammel, M. Leiviskä, V. Petříček, P. Doležal, E. Schmoranzarová, A. Bad'ura, A. Thomas, V. Baltz, L. Míchez, J. Sinova, S. T. B. Goennenwein, T. Jungwirth, and L. Šmejkal, *Macroscopic time reversal symmetry breaking by staggered spin-momentum interaction*, arXiv:2012.15651.
- [39] Z. Feng, X. Zhou, L. Šmejkal, L. Wu, Z. Zhu, H. Guo, R. González-Hernández, X. Wang, H. Yan, P. Qin, X. Zhang, H. Wu, H. Chen, Z. Meng, L. Liu, Z. Xia, J. Sinova, T. Jungwirth, and Z. Liu, *An anomalous Hall effect in altermagnetic ruthenium dioxide*, *Nat. Electron.* **5**, 735 (2022).
- [40] R. D. Gonzalez Betancourt, J. Zubáč, R. Gonzalez-Hernandez, K. Geishendorf, Z. Šobáň, G. Springholz, K. Olejník, L. Šmejkal, J. Sinova, T. Jungwirth, S. T. B. Goennenwein, A. Thomas, H. Reichlová, J. Železný, and D. Kriegner, *Spontaneous anomalous Hall effect arising from an unconventional compensated magnetic phase in a semiconductor*, *Phys. Rev. Lett.* **130**, 036702 (2023).
- [41] L. Šmejkal, A. H. MacDonald, J. Sinova, S. Nakatsuji, and T. Jungwirth, *Anomalous Hall antiferromagnets*, *Nat. Rev. Mater.* **7**, 482 (2022).
- [42] I. I. Mazin, *Notes on altermagnetism and superconductivity*, arXiv:2203.05000.
- [43] L. Šmejkal, A. Marmodoro, K.-H. Ahn, R. Gonzalez-Hernandez, I. Turek, S. Mankovsky, H. Ebert, S. W. D'Souza, O. Šipr, J. Sinova, and T. Jungwirth, *Chiral magnons in altermagnetic RuO₂*, *Phys. Rev. Lett.* **131**, 256703 (2023).
- [44] I. Mazin (PRX Editors), *Editorial: Altermagnetism—A new punch line of fundamental magnetism*, *Phys. Rev. X* **12**, 040002 (2022).
- [45] M. Costa and P. Brown, *Magnetisation density in MnF₂*, *Physica (Amsterdam)* **156–157B**, 329 (1989).
- [46] Note that for altermagnetism it is not only important to have the aspherical magnetization density, but also the particular spin symmetry among the opposite aspherical magnetization densities is crucial. The opposite magnetization densities in altermagnets are also needed to be globally inequivalent.
- [47] J. Baruchel, A. Draperi, M. E. Kadir, G. Fillion, M. Maeder, P. Molho, and J. L. Porteseil, *Piezomagnetism and domains in MnF₂*, *J. Phys. (Paris), Colloq.* **49**, C8-1895 (1988).
- [48] H.-Y. Ma, M. Hu, N. Li, J. Liu, W. Yao, J.-F. Jia, and J. Liu, *Multifunctional antiferromagnetic materials with giant piezomagnetism and noncollinear spin current*, *Nat. Commun.* **12**, 2846 (2021).
- [49] I. I. Mazin, K. Koepernik, M. D. Johannes, R. González-Hernández, and L. Šmejkal, *Prediction of unconventional magnetism in doped FeSb₂*, *Proc. Natl. Acad. Sci. U.S.A.* **118**, e2108924118 (2021).
- [50] W. de Haas, B. Schultz, and J. Koolhaas, *Further measurements of the magnetic properties of some salts of the iron group at low temperatures*, *Physica (Utrecht)* **7**, 57 (1940).
- [51] M. S. Seehra and R. E. Helmick, *Anomalous changes in the dielectric constants of MnF₂ near its Néel temperature*, *J. Appl. Phys.* **55**, 2330 (1984).
- [52] Z. Yamani, Z. Tun, and D. H. Ryan, *Neutron scattering study of the classical antiferromagnet MnF₂: A perfect hands-on neutron scattering teaching course*, *Can. J. Phys.* **88**, 771 (2010), <https://cdnsiencepub.com/doi/pdf/10.1139/P10-081>.
- [53] W. H. Baur and A. A. Khan, *Rutile-type compounds. IV. SiO₂, GeO₂ and a comparison with other rutile-type structures*, *Acta Crystallogr. Sect. B* **27**, 2133 (1971).
- [54] J. W. Stout and H. E. Adams, *Magnetism and the third law of thermodynamics. the heat capacity of manganous fluoride from 13 to 320 °K*, *J. Am. Chem. Soc.* **64**, 1535 (1942).
- [55] R. A. Erickson, *Neutron diffraction studies of antiferromagnetism in manganous fluoride and some isomorphous compounds*, *Phys. Rev.* **90**, 779 (1953).
- [56] N. A. Spaldin, M. Fiebig, and M. Mostovoy, *The toroidal moment in condensed-matter physics and its relation to the magnetoelectric effect*, *J. Phys. Condens. Matter* **20**, 434203 (2008).

- [57] F. Bultmark, F. Cricchio, O. Grånäs, and L. Nordström, *Multipole decomposition of LDA + U energy and its application to actinide compounds*, *Phys. Rev. B* **80**, 035121 (2009).
- [58] R. Winkler and U. Zülicke, *Theory of electric, magnetic, and toroidal polarizations in crystalline solids with applications to hexagonal lonsdaleite and cubic diamond*, *Phys. Rev. B* **107**, 155201 (2023).
- [59] C. Ederer and N. A. Spaldin, *Towards a microscopic theory of toroidal moments in bulk periodic crystals*, *Phys. Rev. B* **76**, 214404 (2007).
- [60] S. F. Weber, A. Urru, S. Bhowal, C. Ederer, and N. A. Spaldin, *Surface magnetization in antiferromagnets: Classification, example materials, and relation to magneto-electric responses*, arXiv:2306.06631.
- [61] S. Hayami and M. Yatsushiro, *Spin conductivity based on magnetic toroidal quadrupole hidden in antiferromagnets*, *J. Phys. Soc. Jpn.* **91**, 063702 (2022).
- [62] M. Yatsushiro, H. Kusunose, and S. Hayami, *Multipole classification in 122 magnetic point groups for unified understanding of multiferroic responses and transport phenomena*, *Phys. Rev. B* **104**, 054412 (2021).
- [63] M.-T. Suzuki, T. Nomoto, R. Arita, Y. Yanagi, S. Hayami, and H. Kusunose, *Multipole expansion for magnetic structures: A generation scheme for a symmetry-adapted orthonormal basis set in the crystallographic point group*, *Phys. Rev. B* **99**, 174407 (2019).
- [64] Y. Yanagi, H. Kusunose, T. Nomoto, R. Arita, and M.-T. Suzuki, *Generation of modulated magnetic structures based on cluster multipole expansion: Application to α -mn and CoM_3S_6* , *Phys. Rev. B* **107**, 014407 (2023).
- [65] A. Urru and N. A. Spaldin, *Magnetic octupole tensor decomposition and second-order magnetoelectric effect*, *Ann. Phys. (Amsterdam)* **447**, 168964 (2022).
- [66] F. Cricchio, F. Bultmark, O. Grånäs, and L. Nordström, *Itinerant magnetic multipole moments of rank five as the hidden order in URu_2Si_2* , *Phys. Rev. Lett.* **103**, 107202 (2009).
- [67] M.-T. Suzuki, N. Magnani, and P. M. Oppeneer, *First-principles theory of multipolar order in neptunium dioxide*, *Phys. Rev. B* **82**, 241103(R) (2010).
- [68] F. Cricchio, O. Grånäs, and L. Nordström, *Polarization of an open shell in the presence of spin-orbit coupling*, *Europhys. Lett.* **94**, 57009 (2011).
- [69] A. Mansouri Tehrani and N. A. Spaldin, *Untangling the structural, magnetic dipole, and charge multipolar orders in $\text{Ba}_2\text{MgReO}_6$* , *Phys. Rev. Mater.* **5**, 104410 (2021).
- [70] K. Yamauchi, P. Barone, and S. Picozzi, *Bulk Rashba effect in multiferroics: A theoretical prediction for BiCoO_3* , *Phys. Rev. B* **100**, 245115 (2019).
- [71] S. Bhowal and N. A. Spaldin, *Revealing hidden magneto-electric multipoles using Compton scattering*, *Phys. Rev. Res.* **3**, 033185 (2021).
- [72] S. Bhowal, S. P. Collins, and N. A. Spaldin, *Hidden k -space magnetoelectric multipoles in nonmagnetic ferroelectrics*, *Phys. Rev. Lett.* **128**, 116402 (2022).
- [73] S. Hayami, Y. Yanagi, and H. Kusunose, *Bottom-up design of spin-split and reshaped electronic band structures in antiferromagnets without spin-orbit coupling: Procedure on the basis of augmented multipoles*, *Phys. Rev. B* **102**, 144441 (2020).
- [74] S. Hayami and H. Kusunose, *Essential role of the anisotropic magnetic dipole in the anomalous Hall effect*, *Phys. Rev. B* **103**, L180407 (2021).
- [75] O. K. Andersen and T. Saha-Dasgupta, *Muffin-tin orbitals of arbitrary order*, *Phys. Rev. B* **62**, R16219 (2000).
- [76] A. S. Disa, M. Fechner, T. F. Nova, B. Liu, M. Först, D. Prabhakaran, P. G. Radaelli, and A. Cavalleri, *Polarizing an antiferromagnet by optical engineering of the crystal field*, *Nat. Phys.* **16**, 937 (2020).
- [77] F. Formisano, R. M. Dubrovin, R. V. Pisarev, A. K. Zvezdin, A. M. Kalashnikova, and A. V. Kimel, *Laser-induced THz piezomagnetism and lattice dynamics of antiferromagnets MnF_2 and CoF_2* , *Ann. Phys. (Amsterdam)* **447**, 169041 (2022).
- [78] F. Formisano, R. M. Dubrovin, R. V. Pisarev, A. M. Kalashnikova, and A. V. Kimel, *Laser-induced THz magnetism of antiferromagnetic CoF_2* , *J. Phys. Condens. Matter* **34**, 225801 (2022).
- [79] I. Dzialoshinskii, *The magnetic structure of fluorides of the transition metals*, *Sov. Phys. JETP* **33**, 1454 (1958), http://jetp.ras.ru/cgi-bin/dn/e_006_06_1120.pdf.
- [80] A. S. Borovik-Romanov, *Piezomagnetism in the antiferromagnetic fluorides of cobalt and manganese*, *J. Exp. Theor. Phys.* **38**, 1088 (1960), http://www.jetp.ras.ru/cgi-bin/dn/e_011_04_0786.pdf.
- [81] J. Baruchel, M. Schlenker, and B. Barbara, *180° antiferromagnetic domains in MnF_2 by neutron topography*, *J. Magn. Magn. Mater.* **15–18**, 1510 (1980).
- [82] A. H. Compton, *A quantum theory of the scattering of X-rays by light elements*, *Phys. Rev.* **21**, 483 (1923).
- [83] P. M. Platzman and N. Tzoar, *Magnetic scattering of x rays from electrons in molecules and solids*, *Phys. Rev. B* **2**, 3556 (1970).
- [84] N. Sakai and K. Ôno, *Compton profile due to magnetic electrons in ferromagnetic iron measured with circularly polarized γ rays*, *Phys. Rev. Lett.* **37**, 351 (1976).
- [85] M. J. Cooper, S. P. Collins, S. W. Lovesey, D. Laundry, and D. N. Timms, *Magnetic Compton scattering—Gathering momentum*, *Phys. Scr.* **T35**, 103 (1991).
- [86] J. A. Duffy, J. W. Taylor, S. B. Dugdale, C. Shenton-Taylor, M. W. Butchers, S. R. Giblin, M. J. Cooper, Y. Sakurai, and M. Itou, *Spin and orbital moments in Fe_3O_4* , *Phys. Rev. B* **81**, 134424 (2010).
- [87] M. Itou, A. Koizumi, and Y. Sakurai, *Spin and orbital magnetization loops obtained using magnetic Compton scattering*, *Appl. Phys. Lett.* **102**, 082403 (2013).
- [88] E. Zukowski, S. P. Collins, M. J. Cooper, D. N. Timms, F. Itoh, H. Sakurai, H. Kawata, Y. Tanaka, and A. Malinowski, *The magnetic Compton profile of ferrimagnetic HoFe_2* , *J. Phys. Condens. Matter* **5**, 4077 (1993).
- [89] J. A. Duffy, J. E. McCarthy, S. B. Dugdale, V. Honkimäki, M. J. Cooper, M. A. Alam, T. Jarlborg, and S. B. Palmer, *Spin density in Gd studied by magnetic Compton scattering*, *J. Phys. Condens. Matter* **10**, 10391 (1998).
- [90] J. A. Duffy, S. B. Dugdale, J. E. McCarthy, M. A. Alam, M. J. Cooper, S. B. Palmer, and T. Jarlborg, *Induced spin polarization in ferromagnetic $\text{Gd}_{62.4}\text{Y}_{37.6}$* , *Phys. Rev. B* **61**, 14331 (2000).

- [91] Z. F. Banfield, J. A. Duffy, J. W. Taylor, C. A. Steer, A. Bebb, M. J. Cooper, L. Blaauw, C. Shenton-Taylor, and R. Ruiz-Bustos, *Spin-resolved Compton scattering study of RuSr₂GdCu₂O₈*, *J. Phys. Condens. Matter* **17**, 5533 (2005).
- [92] C. Shenton-Taylor, J. A. Duffy, J. W. Taylor, C. A. Steer, D. N. Timms, M. J. Cooper, and L. V. Blaauw, *Magnetic Compton scattering study of the magnetocaloric material Gd₇Pd₃*, *J. Phys. Condens. Matter* **19**, 186208 (2007).
- [93] J. A. Duffy, *What we can learn from magnetic Compton scattering: Application to the determination of spin polarization*, *J. Phys. Conf. Ser.* **443**, 012011 (2013).
- [94] P. E. Mijnaerends, S. Kaprzyk, B. Barbiellini, Y. Li, J. F. Mitchell, P. A. Montano, and A. Bansil, *Magnetic momentum density, Fermi surface, and directional magnetic Compton profiles in LaSr₂Mn₂O₇ and La_{1.2}Sr_{1.8}Mn₂O₇*, *Phys. Rev. B* **75**, 014428 (2007).
- [95] T. Mizoroki, M. Itou, Y. Taguchi, T. Iwazumi, and Y. Sakurai, *Effects of hole doping in electronic states of La_{1-x}Sr_xMnO₃ probed by magnetic Compton scattering*, *Appl. Phys. Lett.* **98**, 052107 (2011).
- [96] B. L. Ahuja, *Magnetic Compton scattering: A reliable probe to investigate magnetic properties*, *AIP Conf. Proc.* **1512**, 26 (2013).
- [97] J. Taylor and P. Wilson, *The structures of fluorides VI. Precise structural parameters in copper difluoride by neutron diffraction*, *J. Less-Common Met.* **34**, 257 (1974).
- [98] P. Santini and G. Amoretti, *Magnetic-octupole order in neptunium dioxide?*, *Phys. Rev. Lett.* **85**, 2188 (2000).
- [99] Y. Kuramoto and H. Kusunose, *Octupole moment as a hidden order parameter in orbitally degenerate f -electron systems*, *J. Phys. Soc. Jpn.* **69**, 671 (2000).
- [100] H. Kusunose, *Magnetic octupole observed by neutron scattering: A route toward visible order*, *J. Phys. Soc. Jpn. News Comments* **4**, 06 (2007).
- [101] T. Matsumura, T. Yonemura, K. Kunimori, M. Sera, and F. Iga, *Magnetic field induced $4f$ octupole in CeB₆ probed by resonant x-ray diffraction*, *Phys. Rev. Lett.* **103**, 017203 (2009).
- [102] M.-T. Suzuki, T. Koretsune, M. Ochi, and R. Arita, *Cluster multipole theory for anomalous Hall effect in antiferromagnets*, *Phys. Rev. B* **95**, 094406 (2017).
- [103] T. Higo, H. Man, D. B. Gopman, L. Wu, T. Koretsune, O. M. J. van 't Erve, Y. P. Kabanov, D. Rees, Y. Li, M.-T. Suzuki, S. Patankar, M. Ikhlas, C. L. Chien, R. Arita, R. D. Shull, J. Orenstein, and S. Nakatsuji, *Large magneto-optical Kerr effect and imaging of magnetic octupole domains in an antiferromagnetic metal*, *Nat. Photonics* **12**, 73 (2018).
- [104] A. S. Patri, A. Sakai, S. Lee, A. Paramakanti, S. Nakatsuji, and Y. B. Kim, *Unveiling hidden multipolar orders with magnetostriction*, *Nat. Commun.* **10**, 4092 (2019).
- [105] D. D. Maharaj, G. Sala, M. B. Stone, E. Kermarrec, C. Ritter, F. Fauth, C. A. Marjerrison, J. E. Greedan, A. Paramakanti, and B. D. Gaulin, *Octupolar versus Néel order in cubic $5d^2$ double perovskites*, *Phys. Rev. Lett.* **124**, 087206 (2020).
- [106] G. Khaliullin, D. Churchill, P. P. Stavropoulos, and H.-Y. Kee, *Exchange interactions, Jahn-Teller coupling, and multipole orders in pseudospin one-half $5d^2$ Mott insulators*, *Phys. Rev. Res.* **3**, 033163 (2021).
- [107] M. Kimata, N. Sasabe, K. Kurita, Y. Yamasaki, C. Tabata, Y. Yokoyama, Y. Kotani, M. Ikhlas, T. Tomita, K. Amemiya, H. Nojiri, S. Nakatsuji, T. Koretsune, H. Nakao, T.-h. Arima, and T. Nakamura, *X-ray study of ferroic octupole order producing anomalous Hall effect*, *Nat. Commun.* **12**, 5582 (2021).
- [108] S. Voleti, K. Pradhan, S. Bhattacharjee, T. Saha-Dasgupta, and A. Paramakanti, *Probing octupolar hidden order via Janus impurities*, *npj Quantum Mater.* **8**, 42 (2023).
- [109] D. J. Lockwood and M. G. Cottam, *The spin-phonon interaction in FeF₂ and MnF₂ studied by Raman spectroscopy*, *J. Appl. Phys.* **64**, 5876 (1988).
- [110] M. G. Cottam and D. J. Lockwood, *Spin-phonon interaction in transition-metal difluoride antiferromagnets: Theory and experiment*, *Low Temp. Phys.* **45**, 78 (2019).
- [111] V. I. Nizhankovskii, A. I. Kharkovskii, and A. J. Zaleski, *Spontaneous surface magnetisation of single crystal MnF₂ in the antiferromagnetic state*, *Acta Phys. Pol. A* **97**, 487 (2000).
- [112] *The ELK code*, <http://elk.sourceforge.net/>.
- [113] D. Ernstring, D. Billington, T. D. Haynes, T. E. Millichamp, J. W. Taylor, J. A. Duffy, S. R. Giblin, J. K. Dewhurst, and S. B. Dugdale, *Calculating electron momentum densities and Compton profiles using the linear tetrahedron method*, *J. Phys. Condens. Matter* **26**, 495501 (2014).
- [114] A. Urru, J.-R. Soh, N. Qureshi, A. Stunault, B. Roessli, H. M. Rønnow, and N. A. Spaldin, *Neutron scattering from local magnetoelectric multipoles: A combined theoretical, computational, and experimental perspective*, *Phys. Rev. Res.* **5**, 033147 (2023).
- [115] P. E. Blöchl, *Projector augmented-wave method*, *Phys. Rev. B* **50**, 17953 (1994).
- [116] G. Kresse and D. Joubert, *From ultrasoft pseudopotentials to the projector augmented-wave method*, *Phys. Rev. B* **59**, 1758 (1999).
- [117] G. Kresse and J. Hafner, *Ab initio molecular dynamics for liquid metals*, *Phys. Rev. B* **47**, 558 (1993).
- [118] G. Kresse and J. Furthmüller, *Efficient iterative schemes for ab initio total-energy calculations using a plane-wave basis set*, *Phys. Rev. B* **54**, 11169 (1996).
- [119] L. Schaufelberger, M. E. Merkel, A. M. Tehrani, N. A. Spaldin, and C. Ederer, *Exploring energy landscapes of charge multipoles using constrained density functional theory*, *Phys. Rev. Res.* **5**, 033172 (2023).
- [120] M. E. Merkel, *multipyles v1.1.0*, 2023, Zenodo, <https://zenodo.org/records/8199391>.